International Journal of Solids and Structures 81 (2016) 160–178

Contents lists available at ScienceDirect

International Journal of Solids and Structures

journal homepage: www.elsevier.com/locate/ijsolstr

Numerical study of thermo-mechanical coupling effects on crack tip fields of mixed-mode fracture in pseudoelastic shape memory alloys

Saeed Hatefi Ardakani, Arman Afshar, Soheil Mohammadi*

High Performance Computing Laboratory, School of Civil Engineering, University of Tehran, Tehran, Iran

ARTICLE INFO

Article history:
Received 8 August 2015
Revised 28 October 2015
Available online 4 December 2015

Keywords:
Pseudoelastic shape memory alloys
Thermo-mechanical interaction
Applied loading rate
General mixed-mode loading
Plane stress/strain crack tip fields in martensitic region
Crack tip energy release rate

ABSTRACT

The thermo-mechanical coupling effects on mixed-mode crack tip parameters in pseudoelastic shape memory alloys are studied by a finite element solution. Different loading rates are applied on the K-dominant part of the small scale transformation region. Both plane strain and plane stress analyses are carried out to study how the coupling between thermal and mechanical regimes alters the near tip fields in the martensitic region. The crack tip energy release rate and the J-integral remain history-dependent. The stress/strain response, the angular distributions of the stress and the released temperature, the shape of the transformation zone and the released temperature are selected as the crack tip fields of interest. Special attention is given to study of how the aforementioned crack tip fields are affected by the increase of applied loading rate. A comparison is also drawn between the crack tip fields in plane strain and plane stress states to complete the discussion.

1. Introduction

The shape memory effect, or the ability to recover large strains and reverting to the original undeformed shape upon heating, attaches a great deal of importance to shape memory alloys (SMAs), making this type of active materials highly desirable in aerospace, automotive, and biomedical applications. The key to this unique behavior is the non-diffusional martensitic transformation, during which the homogeneous shear lattice movement of atoms changes the crystalline structure. In addition to the shape memory effect, which is a result of phase transformation upon heating, SMAs do possess the pseudoelastic behavior, which is the phase transformation under high applied stresses. Fig. 1 describes the typical pseudoelastic behavior of SMA by depicting a complete loading/unloading stress–strain cycle. Four fundamental temperatures associated with points of change in slope of stress–strain curve, presented in the Fig. 1, are: M_s martensitic start temperature, M_f martensitic finish temperature, A_s austenitic start temperature, and A_f austenitic finish temperature. Corresponding levels of stresses are also defined accordingly. As shown in Fig. 1, loading an SMA specimen above the stress level σ_{MS} with ambient temperature above A_f triggers the forward phase transformation from austenite to martensite, indicated by a change in the slope of the stress/strain curve in the stress level σ_{MS}. Further increase of the loading completes the partial transformation process in point σ_{Mf}, resulting in the fully transformed martensitic crystal, which in general has different macroscopic material properties than the properties of austenite phase. By removing the external loading, the martensitic crystal deforms elastically to stress level σ_{AS}, where the reverse phase transformation initiates. Further unloading completes the reverse transformation at stress level σ_{Af}, recovering the strain and finishing the pseudoelastic cycle.

As discussed earlier, sufficient high stress can trigger the forward phase transformation process in SMA. Therefore, a region in which this phenomenon could happen is the region close to the crack tip, where the existing very high stress levels transform the crystals from austenite to martensite. This phenomenon is illustrated schematically in Fig. 2, in which three distinct regions can be distinguished. One is the austenitic region relatively far from the crack tip where the level of stress is not sufficient enough to trigger phase transformation. By moving closer to the crack tip, the material starts to transform, resulting in a partially transformed region. Finally, in the region close to the crack tip, a fully transformed martensitic region is formed. These transformed zones affect the fracture parameters close to the tip. Therefore, understanding the effect of these fully and partially transformation zones is crucial for fracture analysis and design of SMAs. Since the phase transformation is inherently a thermo-mechanically coupled phenomenon, this study is devoted to study of how the rate of applied loading affects the temperature distribution and, in turn, fracture parameters of SMAs.

A number of experimental studies on fractures in SMAs exist in the literature: Robertson et al. (2007) used Synchrotron X-rays to study strain fields and the martensitic region in front of a propagating

* Corresponding author. Tel.: +98 21 6111 2258; fax: +98 21 6640 3808.
E-mail address: smoham@ut.ac.ir (S. Mohammadi).

http://dx.doi.org/10.1016/j.ijsolstr.2015.11.023
0020-7683/

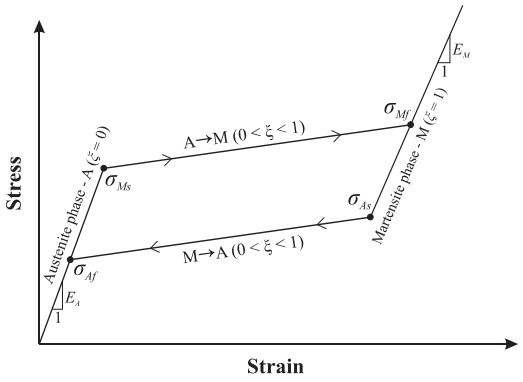

Fig. 1. Stress–strain curve of pseudoelastic behavior of shape memory alloys.

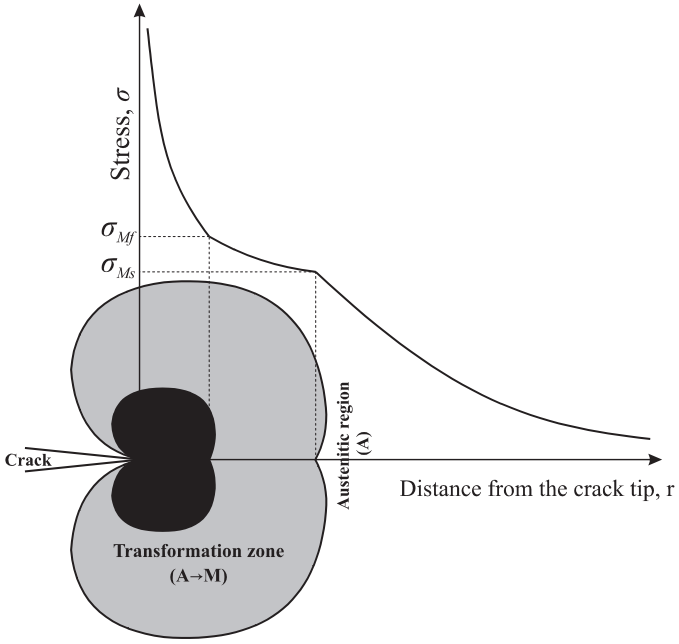

Fig. 2. Stress induced phase transformation in the tip of a crack.

crack under cyclic loading. They found that the deformed martensite constitutes the plastic region in front of the crack tip. Moreover, they came to understanding that the local texture and consequent micromechanics are two key factors affecting the shape of transformation zone in the crack tip vicinity. Gollerthan et al. (2008) and Gollerthan et al. (2009b) examined a compact tension specimen to investigate the shape of the transformation zone ahead of the crack and the effect of this zone on fracture mechanics behavior of the specimen. To study thermal alterations on the material surface, Gollerthan et al. (2009a) employed Infrared thermography and observed that unloading triggers reverse transformation of martensitic regions. Employing a synchrotron beam, it was proved that under plane strain condition, the stress-induced martensite was discernible ahead of the center crack in a CT specimen. Maletta et al. (2014) incorporated full field measurement techniques of Infrared thermography and Digital Image Correlation, to capture the cyclic thermal and mechanical behavior of crack tip along with calculating the corresponding mode I stress intensity factor in a single edge crack specimen.

In addition to experimental studies, theoretical and numerical approaches have been employed to study the effects of transformation zone ahead of the tip of a crack. Yi and Gao (2000) used the crack shielding theory to investigate the toughening effects of the transformation zone in the tip of mode-I crack. Another equally important conclusion of this study was the decrease of crack tip stress intensity factor by increase of temperature. The same work was also extended to the case of mixed mode loading in Yi et al. (2001) indicating that the transformation zone became asymmetric on the grounds of mode-mixity. The effect of reversible phase transformation in decreasing the increased toughness in fracture of SMAs was reported in works of Stam and Van der Giessen (1995) and Freed and Banks-Sills (2007). Xiong and Liu. (2007) utilized a linear elastic fracture mechanics with Irwin's correction to study the thermally induced fracture in Ni–Mn–Ga shape memory alloys showing that as a result of increased cooling rate, the stress intensity factor would experience a significant increase. In another theoretical model, Maletta and Furgiuele (2011) after defining two different stress intensity factors corresponding to stress fields in austenitic and martensitic regions, attempted to investigate the effects of thermo-mechanical parameters on stress intensity factors. Employing the Dugdale–Barenblatt model, Baxevanis and Lagoudas (2012) derived closed form solutions for the size of the transformation zone, the energy release rate and the crack opening displacement (COD) of mode-I stationary cracks, and derived an equation relating the J-integral and the COD.

Also, using the finite element model of Auricchio et al. (1997), which neglected plastic deformation in the tip of crack, Wang et al. (2005) simulated the transformation zone in the crack tip of compact tension (CT) specimens and observed the growth of transformation zone ahead of a crack tip by the increase of the crack length. Wang (2007), however, incorporated the plastic deformation in the numerical model and calculated a 47% increase in fracture toughness due to martensitic transformation. Finally, to numerically investigate the crack propagation phenomena in shape memory alloys, Hatefi Ardakani et al. (2015) utilized the extended finite element approach, determining the crack extension by a stress-based weighted averaging method and considering the thermo-mechanical coupling of these alloys.

Since nearly all available theoretical and numerical studies on the effects of martensitic transformation on fracture of SMAs have neglected the thermo-mechanical couplings, the current study is devoted to analyze the coupling effects of released temperature during the forward phase transformation on crack tip parameters. In fact, this work can be considered as an extension of the work of Baxevanis et al. (2012), in which the effect of martensitic transformation on the J-integral was simulated under the isothermal condition. The current study, however, employs a fully coupled thermo-mechanical constitutive equation to account for such coupling effects, and to investigate the effects of the applied loading rate on crack tip parameters. Although shape memory alloys are not viscous materials, applied loading rate is important due to thermo-mechanical interaction, and should be considered in simulations. Moreover, while the simulation of Baxevanis et al. (2012) was limited to only pure mode cracks in plane strain conditions, both plane strain and plane stress states of general mixed mode fractures are studied here. In addition, while Hatefi Ardakani et al. (2015) focused on extended finite element method (XFEM) and the stress-based crack propagation phenomena in SMAs, this study employs a J-integral approach to investigate the effect of applied loading rates and the corresponding latent heat on the crack tip fields in pseudoelastic SMAs under mixed mode loading conditions.

The present work has the following structure: Section 2 describes the geometry and boundary condition of the considered problem within the framework of small scale transformation zone. It also describes the method utilized for evaluating the energy release rate. Section 3 briefly discusses the adopted continuum thermodynamic based constitutive model, along with its numerical implementation. Section 4 presents the numerical results of the effects of

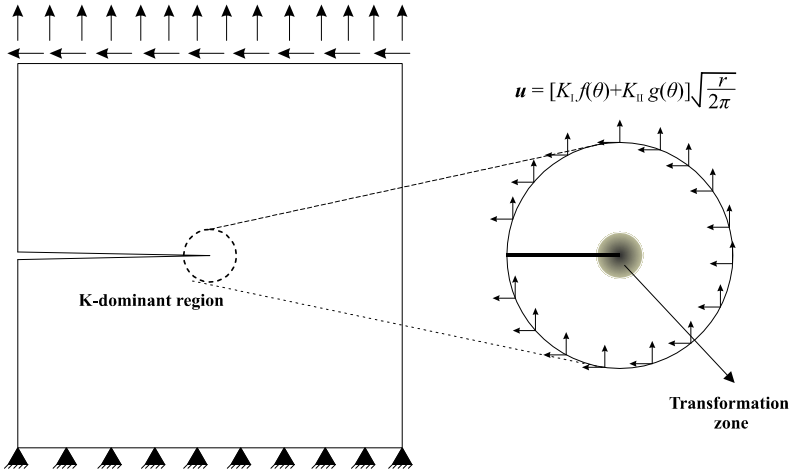

Fig. 3. Mixed-mode fracture analysis of SMA crack tip.

stress-induced phase transformation zone ahead of a crack tip, incorporating thermo-mechanically coupled effects on crack tip energy release rate, stress/strain curve during the loading process, angular distributions of the stress and released temperature, shape of the transformation zone and released temperature. The results are provided for a mixed-mode crack under both plane strain and plane stress states. Finally, Section 5 concludes the paper by a brief discussion of the results.

2. Problem statement

Since the objective of the paper is to study the thermo-mechanically coupling effects on crack tip parameters under mixed-mode conditions, the configuration presented in Fig. 3 is considered. The global specimen is loaded under a mixed-mode condition, resulting in both opening and shearing crack face displacements. Presuming a small scale transformation zone, the displacements of the K-dominant region, i.e. the region in which the stress and displacement can be described by the singular term of the asymptotic expansion, are applied as the boundary condition to the domain of interest. For an isotropic solid, these displacements have the following form:

$$u_1 = \frac{K_I}{2\mu}\sqrt{\frac{r}{2\pi}}\cos\left(\frac{\theta}{2}\right)\left[\kappa - 1 + 2\sin^2\left(\frac{\theta}{2}\right)\right] + \frac{K_{II}}{2\mu}\sqrt{\frac{r}{2\pi}}\sin\left(\frac{\theta}{2}\right)\left[\kappa + 1 + 2\cos^2\left(\frac{\theta}{2}\right)\right] \quad (1)$$

$$u_2 = \frac{K_I}{2\mu}\sqrt{\frac{r}{2\pi}}\sin\left(\frac{\theta}{2}\right)\left[\kappa + 1 - 2\cos^2\left(\frac{\theta}{2}\right)\right] - \frac{K_{II}}{2\mu}\sqrt{\frac{r}{2\pi}}\cos\left(\frac{\theta}{2}\right)\left[\kappa - 1 - 2\sin^2\left(\frac{\theta}{2}\right)\right] \quad (2)$$

where K_I and K_{II} are pure modes stress intensity factors, μ is the shear modulus, and κ is a constant

$$\kappa = \begin{cases} 3 - 4\upsilon & \text{plane strain} \\ \dfrac{3-\upsilon}{1+\upsilon} & \text{plane stress} \end{cases} \quad (3)$$

The mode-mixity of the crack tip can be quantified by the phase angle Ψ,

$$\Psi = \tan^{-1}\left(\frac{K_{II}}{K_I}\right) \quad (4)$$

The primary crack tip parameters of interest in this work are the energy release rate, and the stress and temperature distributions. The

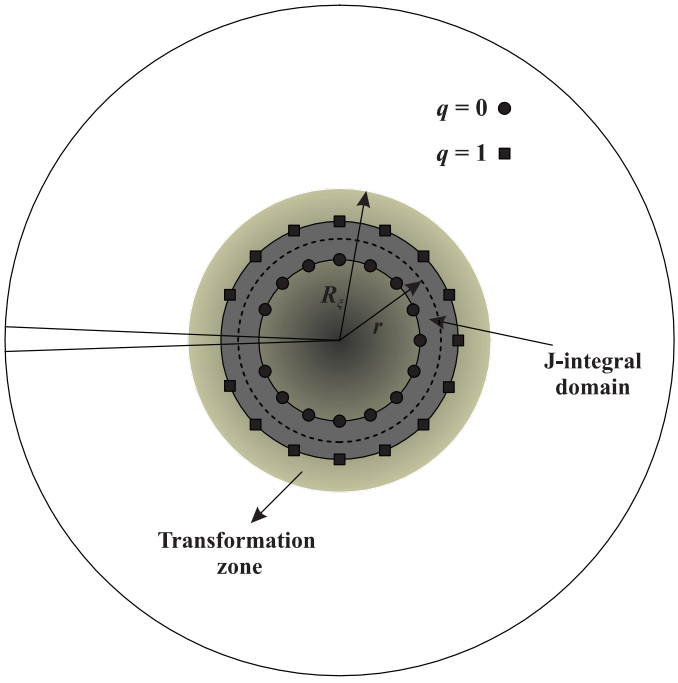

Fig. 4. Q-function for numerical evaluation of J-integral.

energy release rate, G, can be obtained from the J-integral

$$J = \int_\Gamma \left(\mathbf{n}.\boldsymbol{\sigma}.\frac{\partial \mathbf{u}}{\partial x_1} - W n_1\right) ds \quad (5)$$

where Γ is any arbitrary contour surrounding the crack tip, $\mathbf{n}$ is the unit vector normal to Γ, and $W = \int_0^\varepsilon \boldsymbol{\sigma} : d\boldsymbol{\varepsilon}$ is the strain energy density. Numerical implementation of Eq. (5) is carried out using the following equivalent domain integral (Li et al., 1985):

$$J = \int_A \left(\frac{\partial q}{\partial \mathbf{x}}.\boldsymbol{\sigma}.\frac{\partial \mathbf{u}}{\partial x_1} - W\frac{\partial q}{\partial x_1} + \alpha.tr(\boldsymbol{\sigma}).\frac{\partial T}{\partial x_1}.q\right) dA - \int_A \mathbf{f}.\frac{\partial \mathbf{u}}{\partial x_1}.q dA - \int_{C^+ + C^-} \mathbf{t}.\frac{\partial \mathbf{u}}{\partial x_1}.q dC \quad (6)$$

where $\mathbf{t}$ and $\mathbf{f}$ are traction on the crack surface and body force per unit volume, respectively, which, in this study, are considered to be zero. Also, q is an arbitrary function which, as depicted in Fig. 4, by moving from the interior region A to the outer boundary varies from $q = 1$

to $q = 0$. In an isotropic homogeneous solid, the J-integral is path-independent, resulting in the same value if the radius of the contour ($r$in Fig. 4) is changed. In shape memory alloys, however, a zone of transformation in the crystalline structure occurs near the tip of the crack which in turn results in a material with significant different mechanical properties. As a result, the conventional J-integral loses its path-independent nature in the transformation zone. Nonetheless, J-integral retains its path-independent characteristic in farther distances from the crack tip. The corresponding energy release rate can be presented as,

$$G_{\text{applied}} = \frac{1}{E'}\left(K_{\text{I}}^2 + K_{\text{II}}^2\right)$$
$$\begin{cases} E' = E_A \text{ Plane stress} \\ E' = \dfrac{E_A}{1-\upsilon^2} \text{ Plane strain} \end{cases} \tag{7}$$

While similar studies utilized singular elements in the vicinity of the crack tip to reproduce singular stress and strain fields, the partition of unity crack tip enriched elements are assumed here to capture the local stress and displacement distributions. The displacement in the crack tip element has the following form:

$$\mathbf{u} = \sum_i N_i u_i + \sum_i N_i \left(\sum_k f_k a_{ik} \right) \tag{8}$$

where a_{ik} are the additional degrees of freedom for enriching the crack tip element with the following four functions:

$$f(r,\theta) = \left\{ \sqrt{r}\sin\left(\frac{\theta}{2}\right), \sqrt{r}\cos\left(\frac{\theta}{2}\right), \sqrt{r}\sin(\theta)\sin\left(\frac{\theta}{2}\right), \sqrt{r}\sin(\theta)\cos\left(\frac{\theta}{2}\right) \right\} \tag{9}$$

where r and θ are polar coordinates measured from the crack tip.

3. Thermo-mechanical constitutive model of SMA

Having defined the method by which the crack tip parameters are determined, this section is devoted to the description of thermo-mechanically fully coupled constitutive response of SMAs. A number of studies have been carried out on constitutive behavior of SMAs. They include the phase diagram based works of Bekker and Brinson (1997), Govindjee and Kasper (1999), Auricchio et al. (1997), and Lubliner and Auricchio (1996), the Helmholtz free energy based works of Paiva et al. (2005), Anand and Gurtin (2003), Abeyaratne and Knowles (1993), Helm and Haupt (2003), and Reese and Christ (2008), and the Gibbs free energy based works of Boyd and Lagoudas (1996), Raniecki and Lexcellent (1998), Bo and Lagoudas (1999), Popov and Lagoudas (2007), Lagoudas and Entchev (2004), and Ahmadian et al. (2015). The fully coupled model of Boyd and Lagoudas (1996) is adopted here to represent the constitutive response of SMAs.

3.1. Kinematics of deformation

The additive decomposition rule of the infinitesimal strain theory defines the total strain in terms of the thermo-elastic and the transformation components,

$$\varepsilon^{\text{total}} = \varepsilon^{\text{thermo-elastic}} + \varepsilon^{\text{t}} \tag{10}$$

where $\varepsilon^{\text{thermo-elastic}}$ and ε^{t} are the thermo-elastic and the transformation parts of the total strain, respectively. Note that the plastic strain is neglected in the decomposition form of Eq. (10) due to the fact that the plastic deformation constitutes a very small portion of the deformation of the fully-transformed martensitic zone (see Baxevanis et al. (2012)).

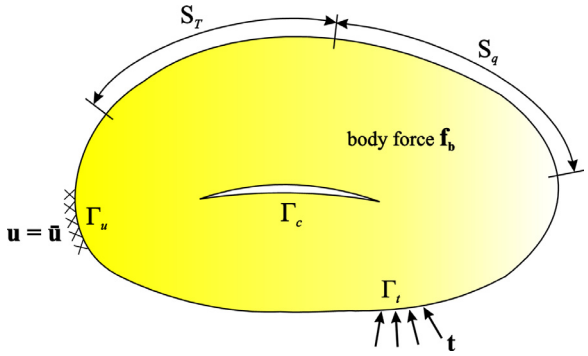

Fig. 5. A typical cracked SMA and boundary conditions.

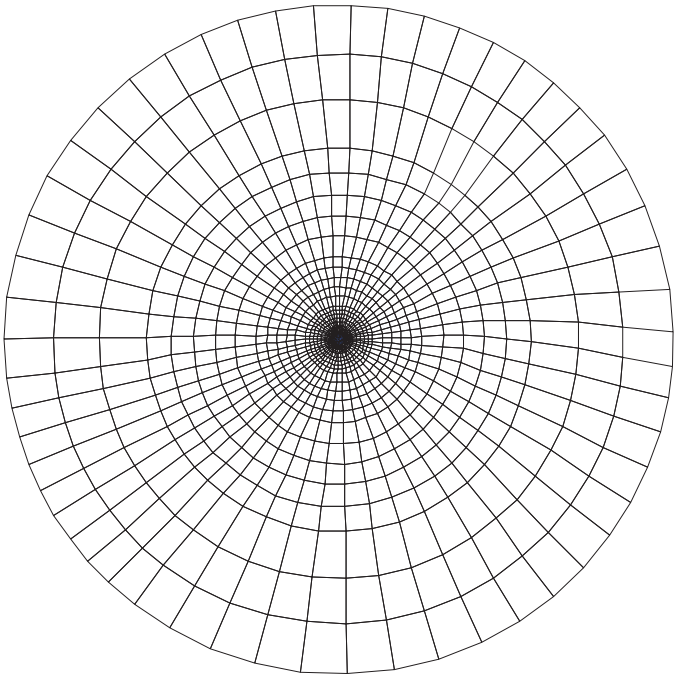

Fig. 6. The finite element mesh.

3.2. Thermodynamic potential

Assuming the external state variables of stress tensor $\boldsymbol{\sigma}$, the transformation strain ε^{t} and the temperature T, and the martensitic volume fraction ξ as the internal state variable, the specific Gibbs free energy, proposed by Boyd and Lagoudas (1996) and Qidwai and Lagoudas (2000), can be written as

$$G_{\text{s}}(\boldsymbol{\sigma}, T, \varepsilon^{\text{t}}, \xi) = -\frac{1}{2\rho}\boldsymbol{\sigma} : \mathbf{S} : \boldsymbol{\sigma} - \frac{1}{\rho}\boldsymbol{\sigma} : \left(\boldsymbol{\alpha}(T - T_0) + \varepsilon^{\text{t}}\right) + c\left((T - T_0) - T\ln\left(\frac{T}{T_0}\right)\right) - s_0 T + u_0 + \frac{1}{\rho}\eta(\xi) \tag{11}$$

where $\mathbf{S}$, $\boldsymbol{\alpha}$, c, ρ, u_0, s_0, andT_0 are the effective compliance tensor, the effective thermal expansion tensor, the effective specific heat, the material density, the effective specific internal energy, the effective specific entropy, and the reference temperature, respectively. $\eta(\xi)$ is also a transformation hardening function defined later. During the phase transformation, the effective material properties are defined in the following manner, with $\xi = 0, 1$ representing the pure austenite (A) and martensitic (M) phases, respectively

(Boyd and Lagoudas, 1996):

$$\mathbf{S}(\xi) = \mathbf{S}^{\mathrm{A}} + \xi\left(\mathbf{S}^{\mathrm{M}} - \mathbf{S}^{\mathrm{A}}\right) \tag{12.1}$$

$$\boldsymbol{\alpha}(\xi) = \boldsymbol{\alpha}^{\mathrm{A}} + \xi\left(\boldsymbol{\alpha}^{\mathrm{M}} - \boldsymbol{\alpha}^{\mathrm{A}}\right) \tag{12.2}$$

$$c(\xi) = c^{\mathrm{A}} + \xi\left(c^{\mathrm{M}} - c^{\mathrm{A}}\right) \tag{12.3}$$

$$s_0(\xi) = s_0^{\mathrm{A}} + \xi\left(s_0^{\mathrm{M}} - s_0^{\mathrm{A}}\right) \tag{12.4}$$

$$u_0(\xi) = u_0^{\mathrm{A}} + \xi\left(u_0^{\mathrm{M}} - u_0^{\mathrm{A}}\right) \tag{12.5}$$

Now, the total small strain can be obtained from the specific Gibbs free energy (Boyd and Lagoudas, 1996) by

$$\boldsymbol{\varepsilon} = -\rho\frac{\partial G_{\mathrm{s}}}{\partial \boldsymbol{\sigma}} = \mathbf{C} : \boldsymbol{\sigma} + \boldsymbol{\alpha}(T - T_0) + \boldsymbol{\varepsilon}^t \tag{13}$$

Finally, the hardening function proposed by Boyd and Lagoudas (1996) is utilized in this work

$$\eta(\xi) = \frac{1}{2}\rho b^{\mathrm{M}}\xi^2 + (\mu_1 + \mu_2)\xi \tag{14}$$

where b^{M}, μ_1, andμ_2 are dependent material properties,

$$b^{\mathrm{M}} = -\Delta s_0(M_{\mathrm{s}} - M_{\mathrm{f}}) \tag{15.1}$$

$$\mu_1 = \frac{1}{2}\rho\Delta s_0(M_{\mathrm{s}} + A_{\mathrm{f}}) - \rho\Delta u_0 \tag{15.2}$$

$$\mu_2 = \frac{1}{4}\rho\Delta s_0(A_{\mathrm{s}} - A_{\mathrm{f}} - M_{\mathrm{f}} + M_s) \tag{15.3}$$

3.3. Transformation rule

The transformation strain can be related to the martensitic volume fraction through the transformation tensor $\boldsymbol{\Lambda}$

$$\dot{\boldsymbol{\varepsilon}}^t = \boldsymbol{\Lambda}\dot{\xi} \tag{16}$$

During the forward phase transformation ($\dot{\xi} > 0$), the transformation tensor has the following form in the model proposed by Boyd and Lagoudas (1996):

$$\boldsymbol{\Lambda} = \frac{3}{2}H\frac{\boldsymbol{\sigma}_{\mathrm{dev}}}{\sigma_{\mathrm{eff}}} \tag{17}$$

where H is the maximum transformation strain. $\boldsymbol{\sigma}_{\mathrm{dev}}$ is the deviatoric stress tensor

$$\boldsymbol{\sigma}_{\mathrm{dev}} = \boldsymbol{\sigma} - \frac{\mathrm{tr}(\boldsymbol{\sigma})}{3}\mathbf{I} \tag{18}$$

and σ_{eff} is the von Mises stress

$$\sigma_{\mathrm{eff}} = \sqrt{\frac{3}{2}\boldsymbol{\sigma}_{\mathrm{dev}} : \boldsymbol{\sigma}_{\mathrm{dev}}} \tag{19}$$

Using the Clausius–Planck inequality, the thermodynamic force Π conjugated to ξ, is defined in the following manner for the specific Gibbs free energy (11):

$$\Pi(\boldsymbol{\sigma}, T, \xi) = \boldsymbol{\sigma} : \boldsymbol{\Lambda} + \frac{1}{2}\boldsymbol{\sigma} : \Delta\mathbf{S} : \boldsymbol{\sigma} + \boldsymbol{\sigma} : \Delta\boldsymbol{\alpha}(T - T_0) - \rho\Delta c\left((T - T_0) - T\ln\left(\frac{T}{T_0}\right)\right) + \rho\Delta s_0 T - \rho\Delta u_0 + \frac{\partial\eta}{\partial\xi} \tag{20}$$

Defining Φ as the transformation surface, the forward phase transformation initiates as Π reaches a critical material parameter X

$$\Phi = \Pi - X = 0 \tag{21}$$

$$X = \frac{1}{4}\rho\Delta s_0(M_{\mathrm{s}} + M_{\mathrm{f}} - A_{\mathrm{s}} - A_{\mathrm{f}}) \tag{22}$$

3.4. Thermo-mechanical coupling effects

The K-dominated region is governed by the mechanical equilibrium equation

$$\nabla.\boldsymbol{\sigma} + \mathbf{f}_{\mathrm{b}} = 0 \tag{23.1}$$

$$\boldsymbol{\sigma}.\mathbf{n} = \mathbf{t}\mathrm{on}\Gamma_{\mathrm{t}} \tag{23.2}$$

$$\mathbf{u} = \bar{\mathbf{u}}\,\mathrm{on}\,\Gamma_{\mathrm{u}} \tag{23.3}$$

with the stress/strain relation in the following incremental form (Lagoudas, 2008):

$$\mathrm{d}\boldsymbol{\sigma} = \mathbf{L} : \mathrm{d}\boldsymbol{\varepsilon} + \boldsymbol{\Theta}\mathrm{d}T \tag{24}$$

where $\mathbf{L}$ is the tangent stiffness tensor and $\boldsymbol{\Theta}$ is the thermal moduli tensor, given as

$$\mathbf{L} = \mathbf{S}^{-1} - \mathbf{A}\otimes\mathbf{A} \tag{25}$$

$$\boldsymbol{\Theta} = -\mathbf{L} : \boldsymbol{\alpha} - \frac{\mathbf{A}}{a}\frac{\partial\Phi}{\partial T} \tag{26}$$

with

$$a = \sqrt{\frac{\partial\Phi}{\partial\boldsymbol{\sigma}} : \mathbf{S}^{-1} : \frac{\partial\Phi}{\partial\boldsymbol{\sigma}} - \frac{\partial\Phi}{\partial\xi}} \tag{27}$$

$$\mathbf{A} = \frac{\mathbf{S}^{-1} : \frac{\partial\Phi}{\partial\boldsymbol{\sigma}}}{a} \tag{28}$$

To solve the discretized form of the equilibrium equation (Eq. (23.1)), $\mathbf{K}\Delta\mathbf{u} = \mathbf{f}^{\mathrm{ext}} - \mathbf{f}^{\mathrm{int}}$, the Newton–Raphson solver is employed using the global tangent stiffness matrix

$$\mathrm{K}_{ij} = \int_{\Omega^{\mathrm{e}}} (\mathbf{B}_i)^T\mathbf{D}\left(\mathbf{B}_j\right)d\Omega \tag{29}$$

$$\mathrm{f}_i^{\mathrm{ext}} = \int_{\Gamma_{\mathrm{t}}} N_i\mathbf{f}^{\mathrm{t}}d\Gamma \tag{30}$$

$$\mathrm{f}_i^{\mathrm{int}} = \int_{\Omega^{\mathrm{e}}} (\mathbf{B}_{\mathrm{i}})^{\mathrm{T}}\boldsymbol{\sigma}d\Omega \tag{31}$$

where $\mathbf{D}$ is the tangent stiffness matrix. First, having calculated the thermo-elastic prediction by

$$\boldsymbol{\sigma}_{n+1}^{(k)} = \left(S_{n+1}^{(k)}\right)^{-1} : \left(\boldsymbol{\varepsilon}_{n+1} - \boldsymbol{\alpha}_{n+1}^{(k)}(T_{n+1} - T_0) - \boldsymbol{\varepsilon}_{n+1}^{\mathrm{t}(k)}\right) \tag{32}$$

Table 1
Applied loading rates ($\dot{G}_{\mathrm{applied}}$) for different phase angles Ψ.

$\dot{G}_{\mathrm{applied}}\left(\frac{\mathrm{N}}{\mathrm{mm.s}}\right)$		$\Psi = 0^\circ$	$\Psi = 15^\circ$	$\Psi = 30^\circ$	$\Psi = 45^\circ$	$\Psi = 60^\circ$	$\Psi = 75^\circ$	$\Psi = 90^\circ$
Plane strain	I	0.88	0.65	0.38	0.24	0.17	0.145	0.138
	II	8.8	6.5	3.8	2.4	1.7	1.45	1.38
	III	88	65	38	24	17	14.5	13.8
Plane stress	I	0.97	0.72	0.42	0.27	0.20	0.164	0.155
	II	9.7	7.2	4.2	2.7	2.0	1.64	1.55
	III	97	72	42	27	20	16.4	15.5

Table 2
SMA properties for the verification simulation.

E_A(GPa)	E_M(GPa)	υ_A	υ_M	H	M_f(°C)	M_s(°C)	C_M(MPa °C^{-1})	T_0(°C)
69	38	0.33	0.33	0.06	46	48	8.7	80

and checking the transformation surface

$$\Phi_{n+1}^{(k)} = \Phi\left(\boldsymbol{\sigma}_{n+1}^{(k)}, T_{n+1}, \xi_{n+1}^{(k)}\right) \tag{33}$$

the cutting plane return mapping algorithm, proposed by (Qidwai and Lagoudas, 2000), is employed to determine the increment of martensitic volume fraction $\Delta\xi_{n+1}^{(k)}$ and the transformation strain $\Delta\boldsymbol{\varepsilon}_{n+1}^{(k)}$, satisfying Eqs. (16) and (21).

$$\Delta\xi_{n+1}^{(k)} = \frac{\Phi_{n+1}^{(k)}}{\frac{\partial\Phi_{n+1}^{(k)}}{\partial\boldsymbol{\sigma}} : \left(S_{n+1}^{(k)}\right)^{-1} : \frac{\partial\Phi_{n+1}^{(k)}}{\partial\boldsymbol{\sigma}} - \frac{\partial\Phi_{n+1}^{(k)}}{\partial\xi}} \tag{34.1}$$

$$\Delta\boldsymbol{\varepsilon}_{n+1}^{(k)} = \Delta\xi_{n+1}^{(k)}\boldsymbol{\Lambda}_{n+1}^{(k)} \tag{34.2}$$

Detailed numerical implementation of this explicit return mapping algorithm can be found in the work of (Qidwai and Lagoudas, 2000) and hence is not repeated here. Calculating the admissible increment in the martensitic volume fraction and the transformation strain, these values are next utilized to solve the fully coupled heat equation in a staggered manner.

Since some latent heat is produced during the forward phase transformation, the coupled heat equation should be solved to account for the coupling effects of temperature (Lagoudas, 2008)

$$T\boldsymbol{\alpha} : \dot{\boldsymbol{\sigma}} + \rho c\dot{T} + (-\Pi + \rho\Delta s_0 T)\dot{\xi} = \nabla.\mathbf{q} \tag{35.1}$$

$$T|_{S_T} = T^s \tag{35.2}$$

$$k_n \left.\frac{\partial T}{\partial \mathbf{n}}\right|_{S_q} = q^s = h(T_{ext}^S - T^S) \tag{35.3}$$

where $\mathbf{q}$ is the heat flow, T^s is the prescribed temperature on surface S_T, $k_n$is the thermal conductivity, $\mathbf{n}$ is the unit normal vector, and q^s is the prescribed heat flux on surface S_q (Fig. 5). Assuming the Fourier's law of heat conduction, the corresponding weak form of Eq. (35.1) can be written as

$$\int_V \delta T\left(T\boldsymbol{\alpha} : \dot{\boldsymbol{\sigma}} + \rho c\dot{T} + (-\pi + \rho\Delta s_0 T)\dot{\xi} - \nabla.(k\nabla T)\right)dV = 0 \tag{36}$$

Applying the divergence theorem leads to

$$\int_V \delta T\boldsymbol{\alpha} : \dot{\boldsymbol{\sigma}} T dV + \int_V \delta T\rho c\dot{T} dV + \int_V \delta T(-\pi + \rho\Delta s_0 T)\dot{\xi} dV = \int_S \delta T((k\nabla T).\mathbf{n})dS - \int_V \nabla\delta T.\nabla(kT)dV \tag{37}$$

Using the convective boundary conditions (35.3) and substituting the following finite element interpolations

$$T = \sum_i N_i T_i \tag{38.1}$$

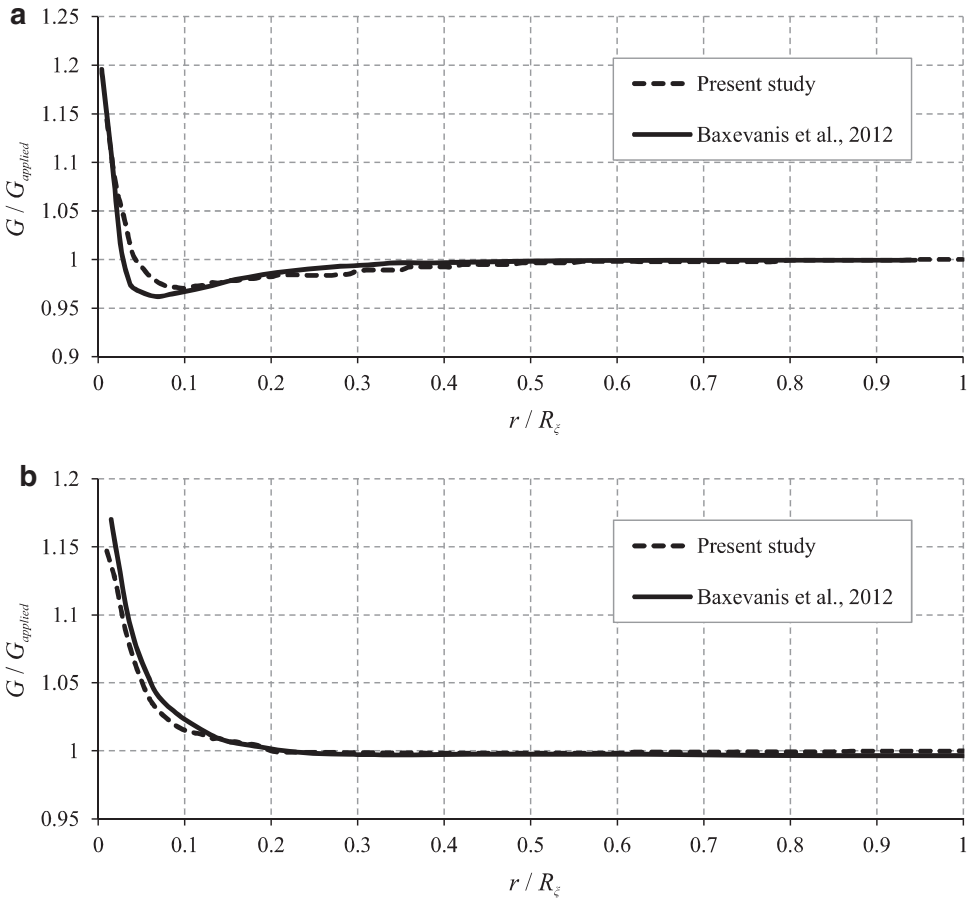

Fig. 7. Verification of the method for pure modes under isothermal conditions (a) $\Psi = 0^\circ$ (mode I), (b) $\Psi = 90^\circ$ (mode II).

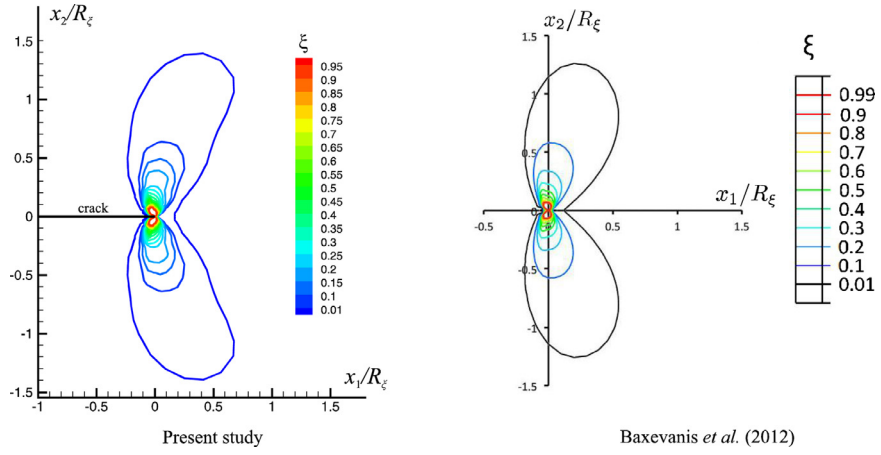

Fig. 8. Comparison of contours of phase transformation between the present study and work by Baxevanis et al. (2012).

$$T_{,i} = \sum_i B_i T_i \tag{38.2}$$

$$\dot{T} = \sum_i N_i \dot{T}_i \tag{38.3}$$

$$T^S = \sum_i N_i T_i^S \tag{38.4}$$

$$\delta T = \sum_i N_i (\delta T)_i \tag{38.5}$$

result in the final discretized form of Eq. (35.1),

$$\left(\mathbf{K} + \mathbf{K}_h + \mathbf{K}_\sigma + \mathbf{K}_\xi\right)T + \mathbf{C}\dot{T} = \mathbf{Q} \tag{39}$$

which can be reformulated in an incremental form

$$\left(\mathbf{K} + \mathbf{K}_h + \mathbf{K}_\sigma^{n+1} + \mathbf{K}_\xi^{n+1}\right)T^{n+1} + \mathbf{C}\frac{T^{n+1} - T^n}{\Delta t} = \mathbf{Q}^{n+1} \tag{40}$$

where the elements of above matrices and vectors are

$$\mathrm{K}_{ij} = \int_\Omega k \nabla N_i \nabla N_j d\Omega \tag{41.1}$$

$$(\mathrm{K}_h)_{ij} = \int_S h N_i N_j dS \tag{41.2}$$

$$(\mathrm{K}_\sigma)_{ij} = \int_\Omega (\boldsymbol{\alpha} : \dot{\boldsymbol{\sigma}}) N_i N_j d\Omega \tag{41.3}$$

$$\left(\mathrm{K}_\xi\right)_{ij} = \int_\Omega \rho \Delta s_0 \dot{\xi} N_i N_j d\Omega \tag{41.4}$$

$$\mathrm{C}_{ij} = \int_\Omega \rho c N_i N_j d\Omega \tag{41.5}$$

$$\mathrm{Q}_i = \int_S h N_i T_{\mathrm{ext}} dS + \int_\Omega \Pi \dot{\xi} N_i d\Omega \tag{41.6}$$

where N is the finite element shape function. Solving Eq. (40) results in the nodal values of the temperature, after which the total out of balance force of the domain is checked

$$\mathbf{R} = \mathbf{f}^{\mathrm{ext}} - \mathbf{f}^{\mathrm{int}} \tag{42}$$

If $\|\mathbf{R}\| > \mathrm{TOL}$, the whole process described in this section is repeated until Eq. (42) is satisfied.

4. Results and discussions

This section presents the results of thermo-mechanical interaction on crack tip fields. After the verification of formulation, detailed effects of applied loading rates on fracture behavior of SMAs are provided. In this work, the applied loading rate is considered as the ratio of applied energy release rate, i.e. far field value (Eq. (7)), to the total time of loading. The energy release rate is computed directly from the J-integral. The ratios considered in this study for each mode-mixity are presented in Table 1.

4.1. Verification

A finite element mesh consisted of 3886 elements, with an increased element density around the crack tip region, is utilized to solve the problem shown in Fig. 6. The transformation zone must be small in comparison to the K-dominated zone in order for the small scale transformation assumption to be valid. In the present case, the K-dominated zone is about 50 times larger than the transformation zone. All dimensions are normalized to the length scale, R_ξ, which

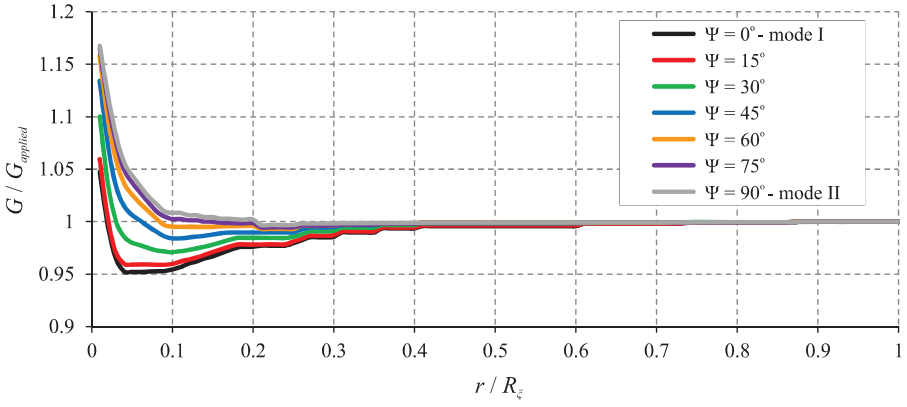

Fig. 9. Comparison of calculated energy release rate for different cases of loading.

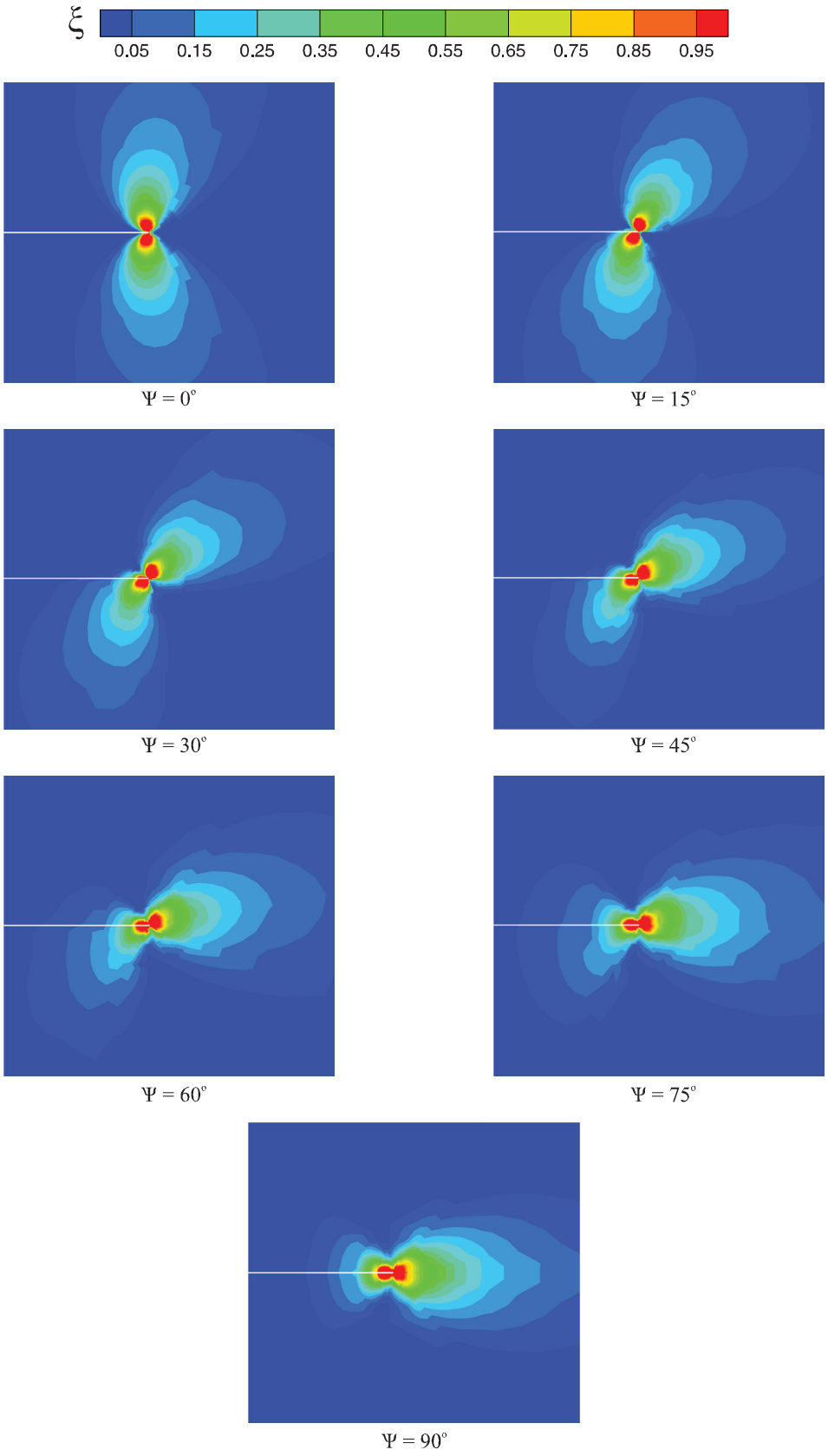

Fig. 10. Rotation of the transformation zone by changing the mode-mixity.

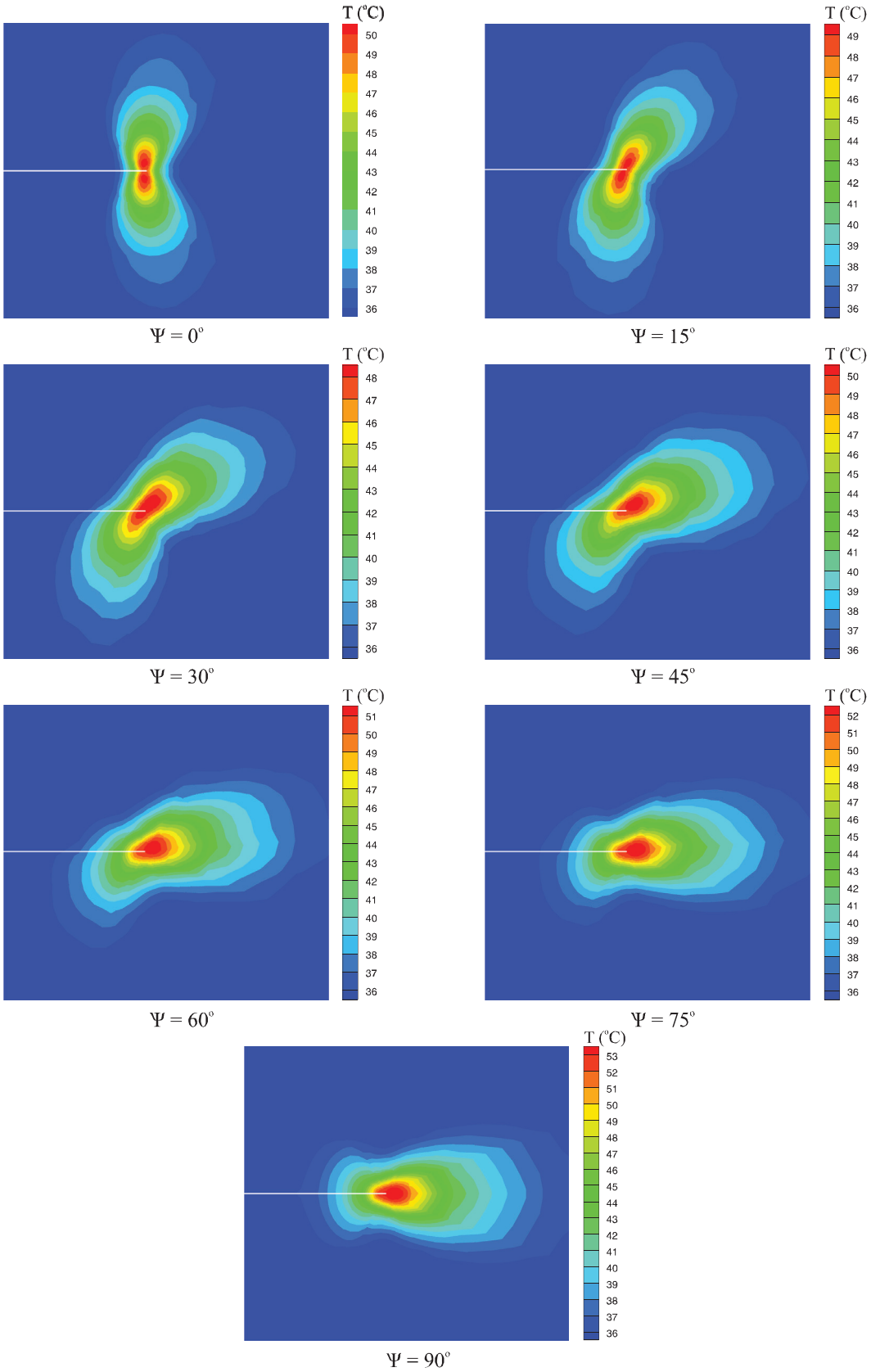

Fig. 11. Rotation of the temperature zone by changing the mode-mixity.

itself is a rough estimation for the half height of the transformation zone in the plane strain state

$$R_\xi = \frac{1}{3\pi}\frac{K_I^2 + 6.25K_{II}^2}{\left(\sigma_{M_s}\right)^2} \tag{43}$$

First, an attempt is made to verify the proposed method. The available work in the literature is the study of individual mode-I and mode-II crack tip fields under the isothermal condition by Baxevanis et al. (2012). The material properties are presented in Table 2.

Fig. 7 shows the normalized energy release rate for contour integrals with different radii based on Eq. (6), and very good agreement exists between the present and reference results. For contour integrals close to the tip of crack, the martensitic transformation of the crystalline structure increases the energy release rate to have a value up to 15–20% larger than the computed value of the far-field J-integral (Eq. (7)). As the radius of the contour integral increases, two distinct trends can be observed. While the mode-I energy release rate decreases to a value smaller than the far-field J-integral and then increases, the mode-II energy release rate has a monotonic decreasing trend towards the far-field value. In larger distances from the crack tip where the material has not been fully transformed, the J-integral regains its path-independent nature and becomes constant. Moreover, a comparison of contours of phase transformation is presented in Fig. 8. It is observed that both the shape and the size of these contours are in good agreement with the work of Baxevanis et al. (2012).

4.2. Analysis under mixed-mode loading incorporating coupling effects

Next, the verified model is used to study the crack tip fields under mixed-mode conditions utilizing the fully coupled thermo-mechanical constitutive relation (Section 3.4). The analysis is performed under plane strain condition first, and then some extensions are made for the case of plane stress. The material properties of SMA are chosen from the work of Baxevanis et al. (2014), and are presented in Table 3. Moreover, to define the thermal boundary condition,

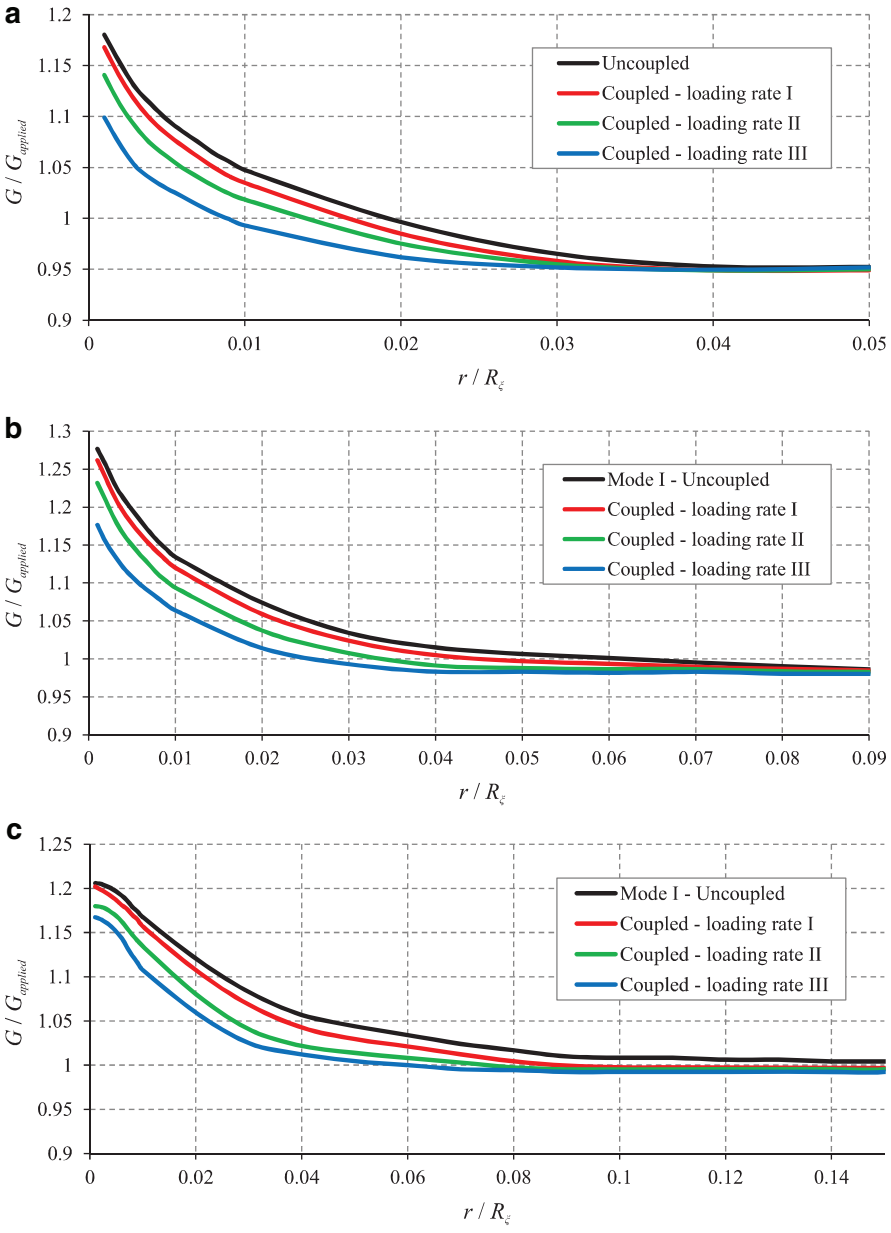

Fig. 12. Effect of applied loading rate in decreasing the energy release rate (a) $\Psi = 0^\circ$, (b) $\Psi = 45^\circ$, (c) $\Psi = 90^\circ$.

Table 3
SMA properties for the mixed mode analysis.

Material parameters	Values	Material parameters	Values
E_A (GPa)	47	T_s^A (°C)	12
E_M (GPa)	24	T_f^A (°C)	26
υ_A	0.33	C_A (MPa°C^{-1})	8.4
υ_M	0.33	C_M (MPa°C^{-1})	6.7
H	0.05	k_n (W.m^{-1}.K^{-1})	18.3
T_0(°C)	35	ρ (kg.m^{-3})	6500
T_f^M (°C)	−29	c (J.kg^{-1}.K^{-1})	837
T_s^M (°C)	3		

prescribed values of ambient temperature are assigned to the perimeter of the circle shown in Fig. 3.

The first objective is to determine how the energy release rate changes as the mode-mixity of the crack tip shifts from pure mode-I to pure mode-II. To this end, the values of K_I and K_{II} in the applied boundary conditions (Eqs. (1) and (2)) are chosen in such a manner that all mixed-mode conditions result in the same value of R_ξ (using Eq. (43)) for all cases. Results of the calculated energy release rates are depicted in Fig. 9, where it can be seen that the curves of mixed-mode loading lie between those of pure mode-I and pure mode-II loading. For mode-mixities of $\Psi = 90^\circ$ and 75°, all values of energy release rate are located above the line $G/G_{applied} = 1$, while in other cases a minimum value below the aforementioned line is observed.

An interesting observation is that the contours of phase transformation follow the applied mode-mixity in the far field. This phenomenon is depicted in Fig. 10, in which it is evident that the shape of the transformation zone follows the phase angle of applied asymptotic boundary condition under different mixed-mode loadings.

Since some latent heat is produced during the process of forward phase transformation, thermo-mechanical coupling effects cannot be ignored in the analysis of crack tip fields. The amount of produced heat during the transformation is a function of both the magnitude and the time span of applied loading. More heat is released during the forward phase transformation by increasing the applied strain rate, having more profound effects on the crack tip fields. Therefore, to account for the effects of applied loading rate, all subsequent mixed mode loading simulations are performed for four cases: three different loading rates and an uncoupled case.

First, the contours of released temperature during the phase transformation are depicted in Fig. 11 for all values of phase angles in the highest strain rate to investigate the shape of the heated zone. As mentioned before, the shape of the heated zone closely follows the shape of the transformation zone for different mixed mode loadings. Experimental observations have been reported by Gollerthan et al. (2009a) and Maletta et al. (2014). However, the difference between their work and the present study could be related to different factors, particularly heat transfer phenomena, applied loading rates and boundary conditions. For instance, the less the applied loading rate, the less the temperature releases. This matter will be fully discussed in Figs. 17 and 22.

Solving the thermo-mechanically coupled equation and calculating the J-integral, it is observed that the latent heat decreases the energy release rate of the crack. For instance, the calculated energy release rates are presented in Fig. 12 for $\Psi = 0^\circ, 45^\circ$and90°. It is observed that the latent heat decreases the available energy for crack growth close to crack tip.

Higher strain rates, which produce more heat in the transformation zone, result in more decrease in the energy release rate. Interesting to note is that in pure mode-I, the coupling effect of latent heat diminishes faster than the case of pure mode-II. While for pure mode-I the effect of latent heat is almost negligible in distances farther than $r/R_\xi = 0.04$, this critical distance is above $r/R_\xi = 0.15$ for pure mode-II simulations.

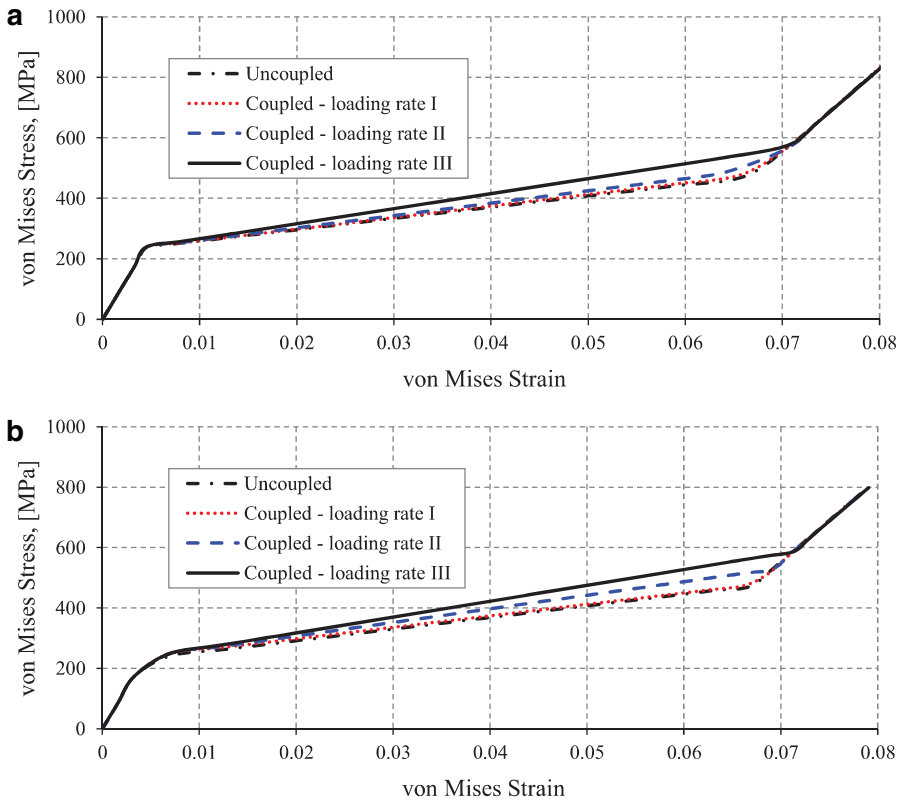

Fig. 13. Effect of the applied loading rate on the level of stress of the partially transformed material (a) $\Psi = 30^\circ$, (b) $\Psi = 60^\circ$.

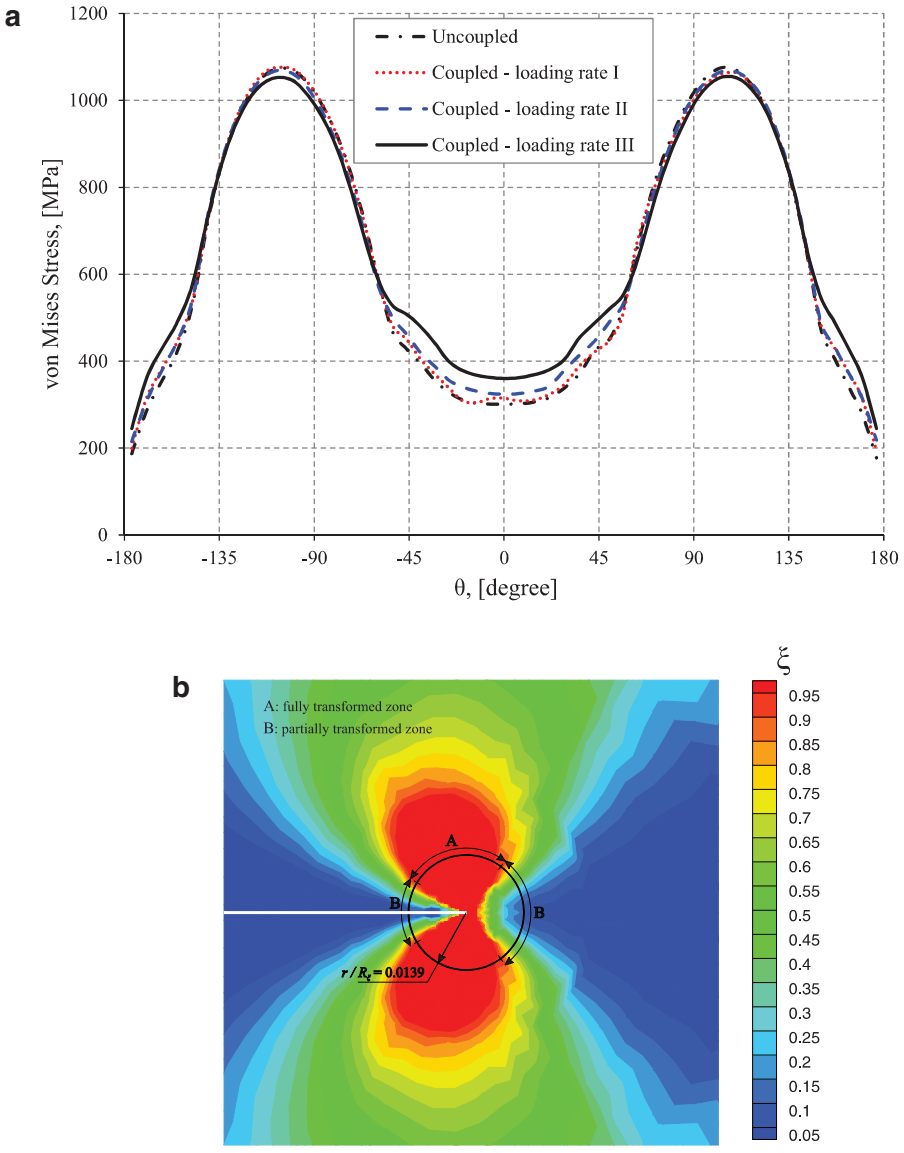

Fig. 14. (a) Effect of the applied loading rate on the level of stress of partially transformed material. (b) Contour of phase transformation near the tip of a plane strain mode-I crack.

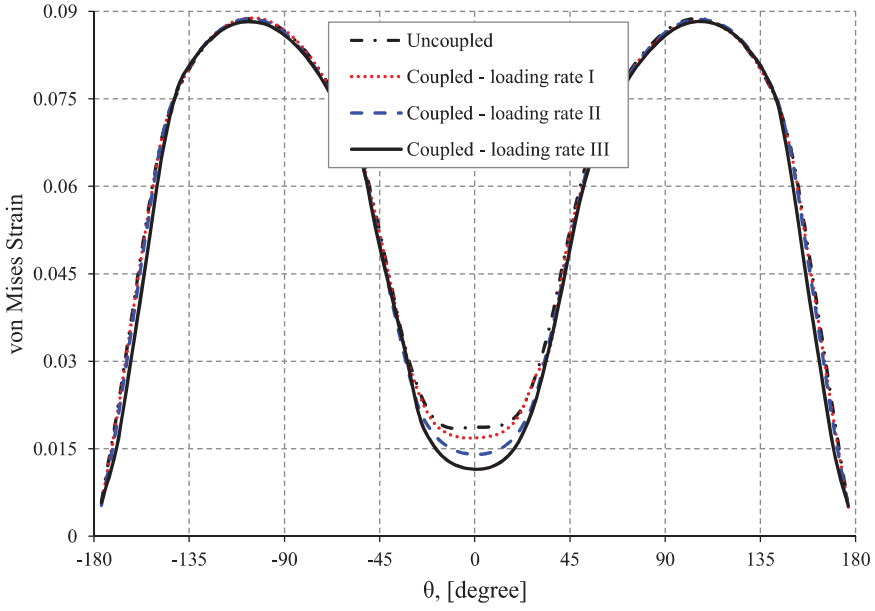

Fig. 15. Strain distribution of the corresponding point for Fig. 14.

Aside from the energy release rate, the coupling effects modify the stress/strain distribution around the crack tip. In two mixed-mode conditions of $\Psi = 30^\circ$ and 60°, the effective stress versus the effective strain curves during the loading process are plotted in Fig. 13 for a point close to the crack tip.

By shortening the time span of applied loading, considerable heat is produced during the forward phase transformation, which increases the stress in steps in which the crystalline structure is partially transformed. The latent heat also increases the finish stress of forward transformation (σ_{M_f}) by an approximate value of 150 MPa for the material properties considered in this study. When the material in the considered point fully transforms into the martensitic phase, no more heat is produced, resulting in the same stress value for all loading rates. Although this trend is depicted only for two mixed-mode conditions, other modes also follow the same pattern.

Moreover, the produced heat alters the angular distribution of stress in points where partial transformation occurs. For the case of pure mode-I, the angular distribution of von Mises stress is depicted in Fig. 14(a) for $r/R_\xi = 0.0139$, where it can be seen that changing applied loading rate only affects stresses of points located in the partial transformation zone and stresses in fully transformed zones are quite insensitive to the applied load rating. As depicted in Fig. 14(b), in pure mode-I, the partially transformed zone lies in front of the crack ($-45^\circ < \theta < 45^\circ$, approximately) and behind the crack tip ($-180^\circ < \theta < -150^\circ$ and $150^\circ < \theta < 180^\circ$, approximately), the angles in which the stress is sensitive to rate of applied loading rates.

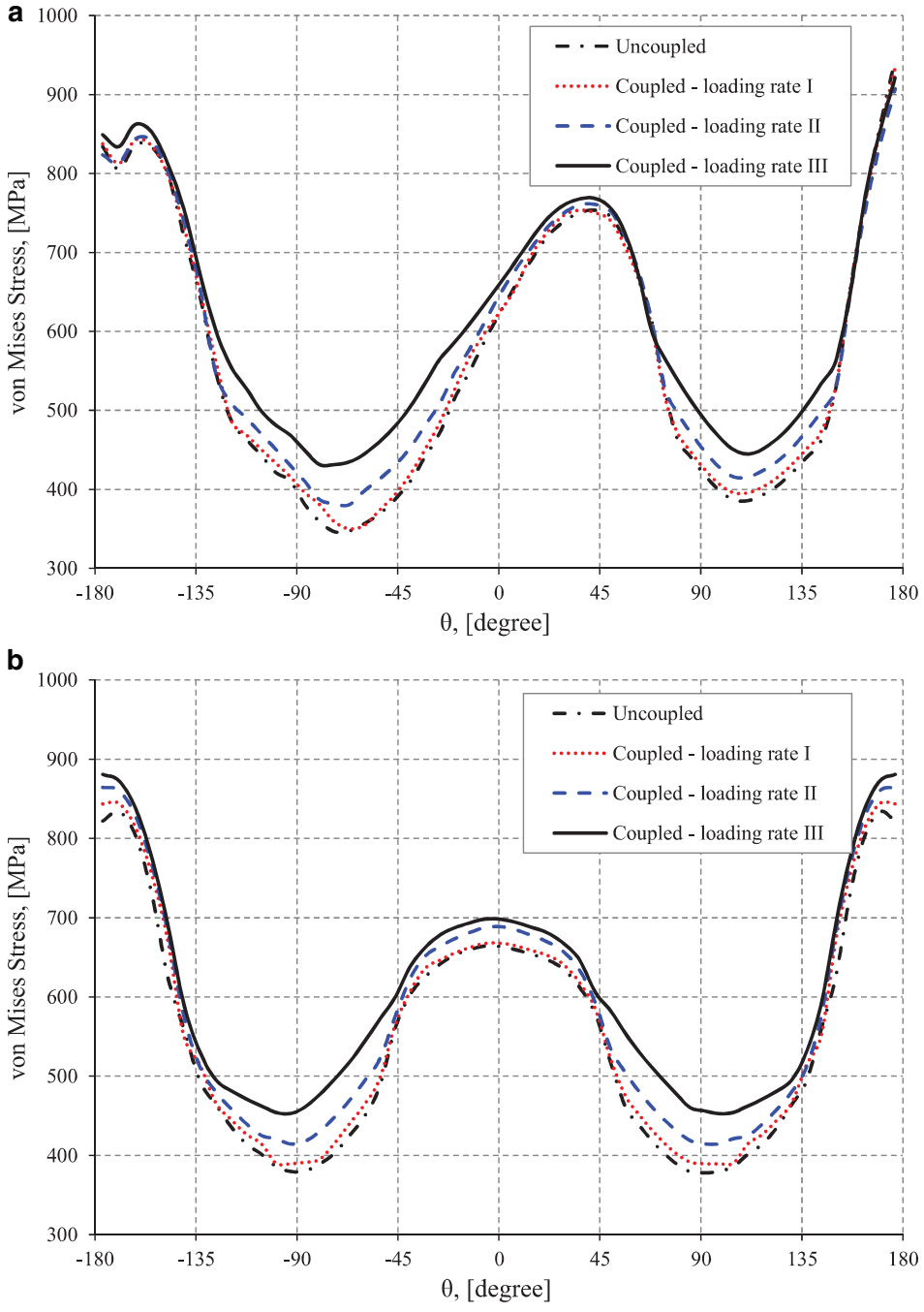

Fig. 16. Effect of the applied loading rate on distribution of the effective stress (a) $\Psi = 60^\circ$, (b) $\Psi = 90^\circ$.

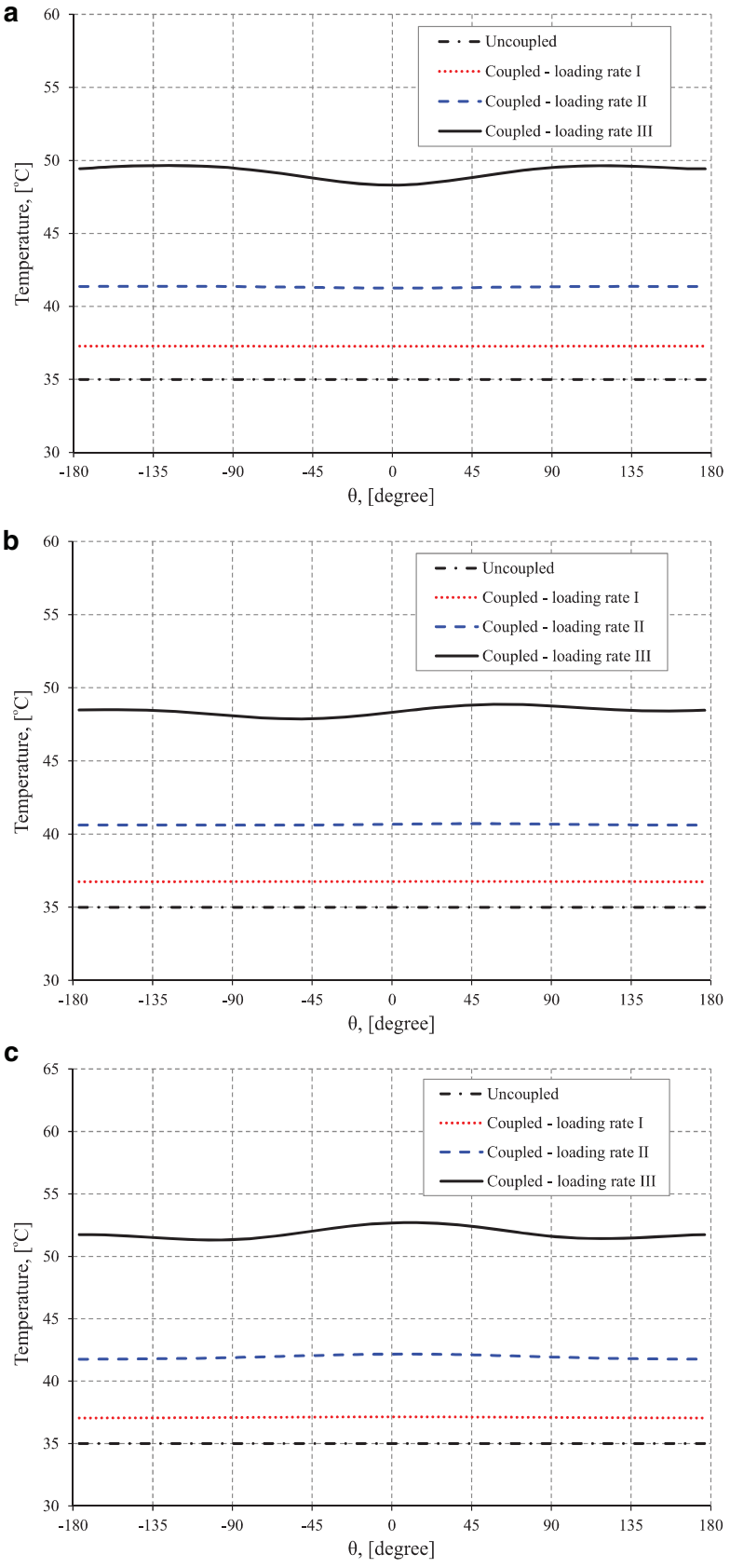

Fig. 17. Effect of applied load rate on the angular variation of temperature around the crack tip (a) $\Psi = 0^{\circ}$, (b) $\Psi = 30^{\circ}$, (c) $\Psi = 75^{\circ}$.

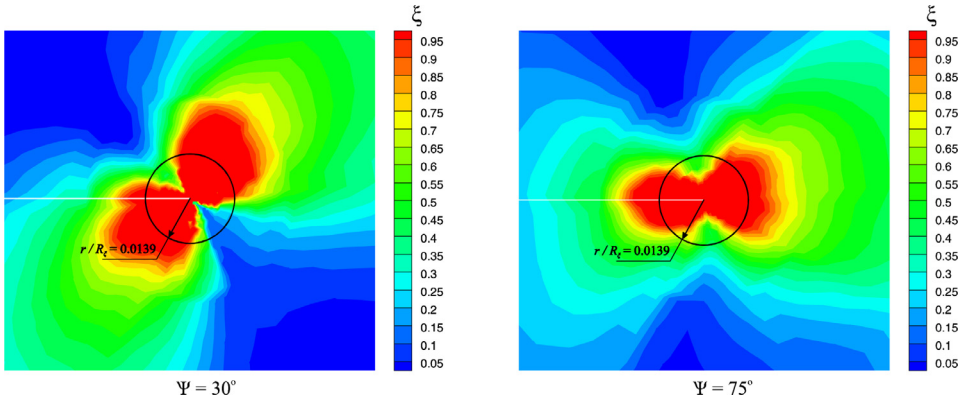

Fig. 18. Contour of phase transformation around the tip of plane strain crack in mode-mixities of $\Psi = 30^\circ$ and $\Psi = 75^\circ$.

Fig. 15 is provided to more clarify this point. It can be seen that in angles where strain is different, e.g. $-30^\circ < \theta < +30^\circ$, stress (Fig. 14(a)) is naturally different. In angles where strain is similar, e.g. $-45^\circ < \theta < -30^\circ$ and $+30^\circ < \theta < +45^\circ$, the point undergoes partial transformation, resulting in different stress as the constitutive behavior (Fig. 13) predicts. Finally, in points located in fully transformed region where strain is similar, the same constitutive behavior, Fig. 13, predict a similar stress.

The same analysis has also been performed for phase angles of $\Psi = 60^\circ$ and $\Psi = 90^\circ$, and the calculated von Mises stresses are plotted in Fig. 16. It can be seen that the released heat affects the angular distribution of effective stress.

In addition to the angular distribution of stress, angular variation of temperature is affected by the rate of applied loading. These variations are depicted in Fig. 17 for pure mode-I, $\Psi = 30^\circ$ and $\Psi = 75^\circ$. The considered point is located in $r/R_\xi = 0.0139$ and in the last mechanical loading step. In the uncoupled case, all points around the crack have the same temperature equal to the ambient temperature, and by increasing the applied loading rate, heat is released in the region which is in the process of forward transformation, resulting in a relatively uniform increase in the temperature of region close to the crack tip. However, the angular variation loses its uniformity in higher loading rates. The reason of this inhomogeneous variation in higher rates of loading can be attributed to the fact that the heat released from points with partial transformed region in these loading rates does not have enough time to reach the considered radius. By analyzing Fig. 14(b), in which the transformation region near the mode-I crack tip is depicted, it can be seen that points behind and in front of the crack tip ($-45^\circ < \theta < 45^\circ$, $-180^\circ < \theta < -150^\circ$ and $150^\circ < \theta < 180^\circ$) are partially transformed, while points located above and below the crack ($-180^\circ < \theta < -50^\circ$ and $50^\circ < \theta < 180^\circ$) have completed the forward phase transformation. In slow loading rates, the heat has time to reach farther points, so the heat released from both the fully and partially transformed regions have time to reach the considered radius of $r/R_\xi = 0.0139$, making the temperature distribution uniform. In faster loading rates, however, the heat releases earlier from fully transformed regions (since these regions have completed partial transformation) and has more time to diffuse to other points. The heat from partial transformed zones, on the other hand, is being released in later loading steps and has only a short time for conduction, leaving the points in front of the crack tip colder. If the thermal equation is allowed to be solved after the last step of applying the mechanical loading, the temperature variation of highest loading rates also becomes uniform. An analogous explanation can also be provided for inhomogeneous temperature variation of high loading rates in other mixed-mode conditions (zoomed-in contours of transformation zone are provided in Fig. 18 for phase angles $\Psi = 30^\circ$ and $\Psi = 75^\circ$).

In order to generalize the argument and make comparison, the previous analysis is now extended to the plane stress case. Only the crack tip values that show different trend with respect to plane strain case are provided. First, for the sake of comparison between different mixed-mode conditions, the energy release rate is calculated for all modes under the isothermal condition and the results are provided in Fig. 19. It is observed that in the small radii close to the crack tip, the material fully transforms to the martensitic phase, resulting in the

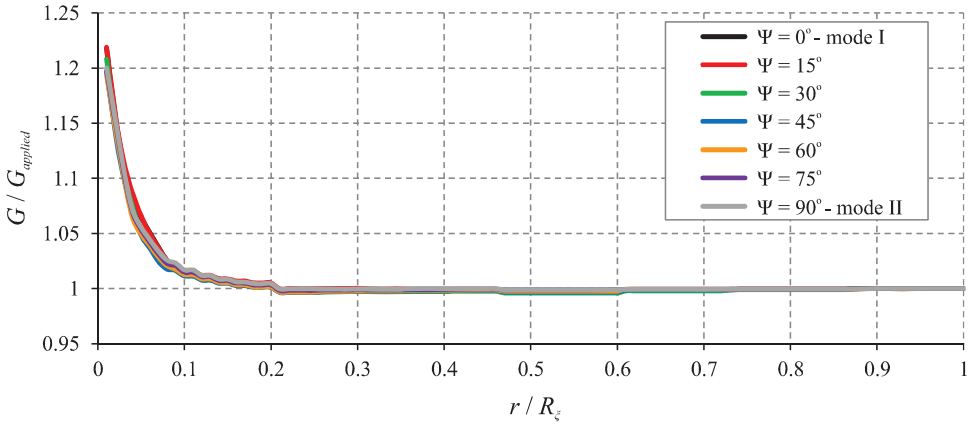

Fig. 19. Comparison of calculated energy release rate for different cases of loading.

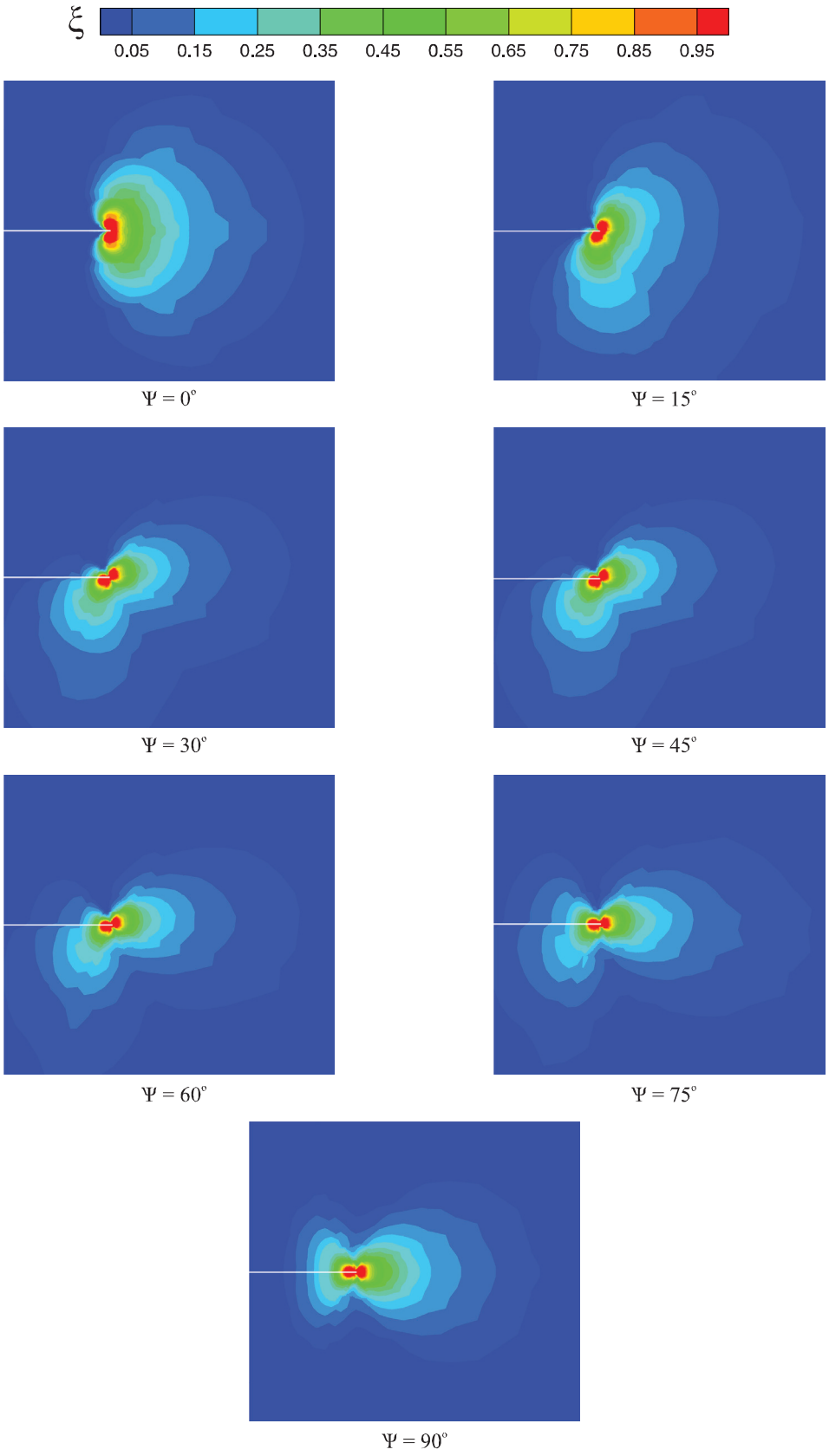

Fig. 20. Rotation of the transformation zone by changing the mode-mixity.

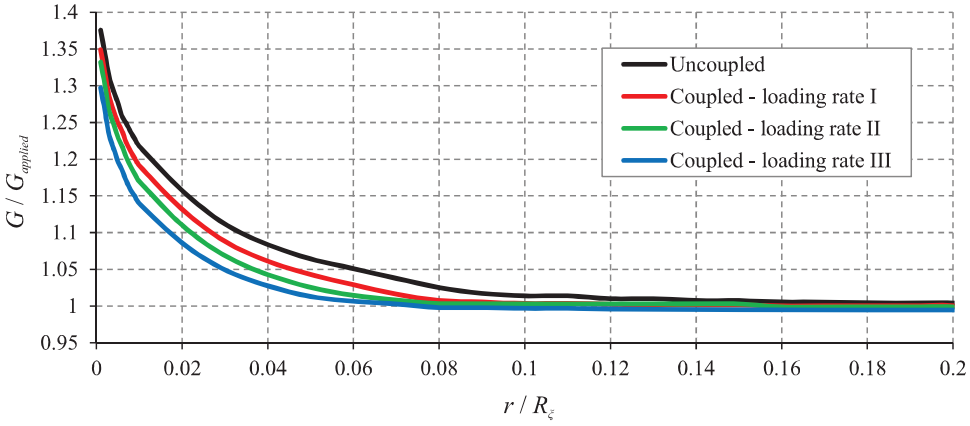

Fig. 21. Effect of the applied loading rate on the energy release rate for case of $\Psi = 0^{\circ}$.

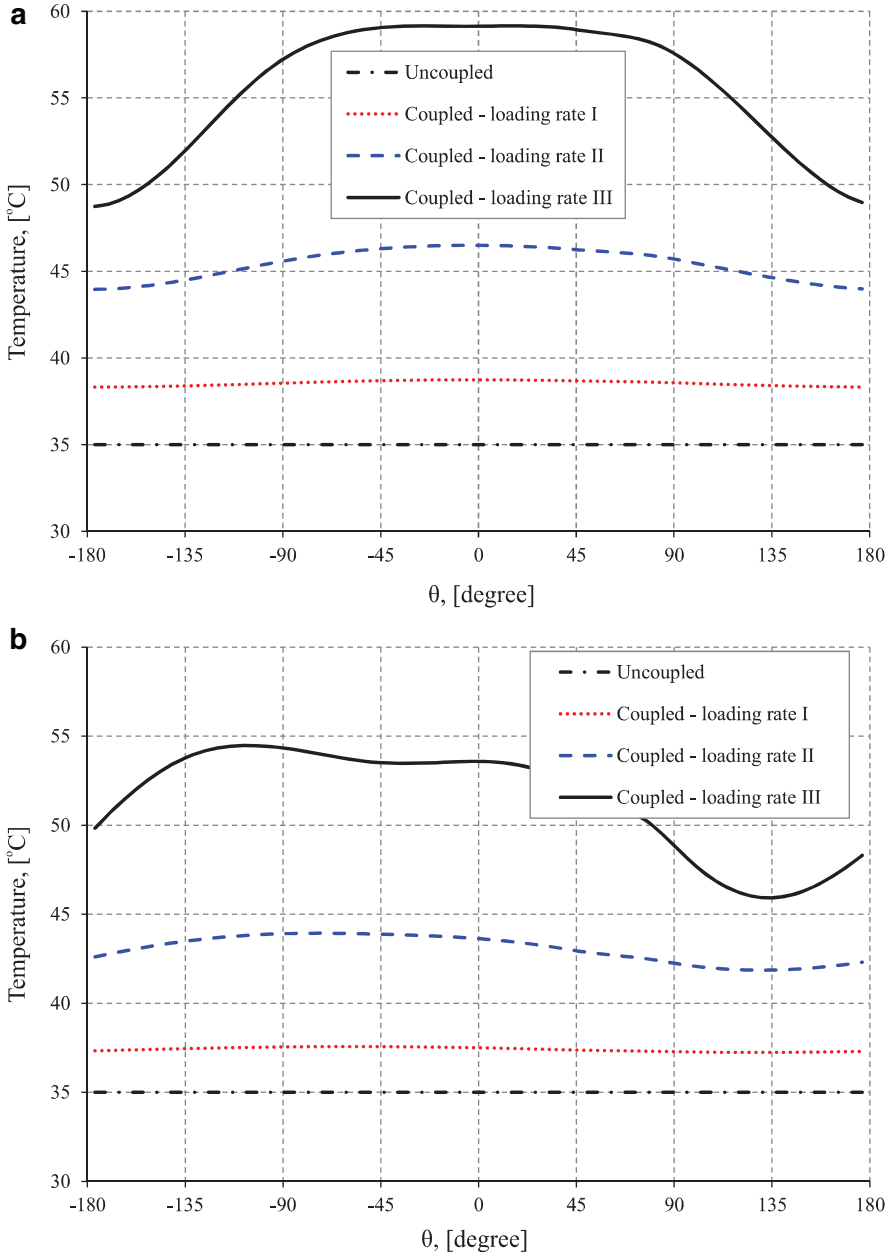

Fig. 22. Effect of the applied loading rate on the angular variation of temperature around the crack tip (a) $\Psi = 0^{\circ}$, (b) $\Psi = 30^{\circ}$.

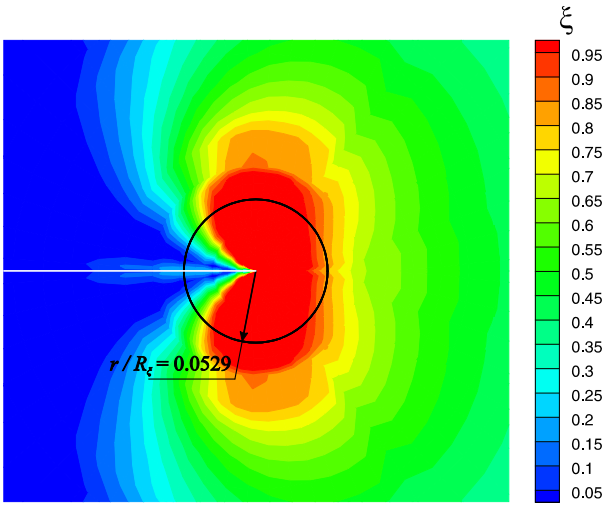

Fig. 23. Contour of phase transformation around the tip of a plane stress mode-I crack.

growth of energy release rate. Important to note is the fundamental dissimilarity between the trend of energy release rate in plane strain and plane stress conditions. While in the plane strain condition the energy release rate might have values lower than the far field energy release rate (see Fig. 9), $G/G_{applied}$ is always greater than unity in the plane stress condition. Furthermore, contours of the transformation zone for the isothermal condition for the highest strain rate are presented in Fig. 20, respectively. Same patterns have been reported by Maletta et al. (2013), in which the finite element method was employed to present the shape of transformation zones for two different values of ambient temperature. A comparison between the shapes of the transformation zone in two cases of plane strain and plane stress reveals the fact that the shape of transformation zone differs between the two stress states. In mode-I, for instance, the transformation zone mostly occupies the upper and lower region of the crack tip in plane strain condition, but the transformation zone in plane stress state is concentrated mainly in the front of the crack tip.

Fig. 21 is provided to show the thermo-mechanical coupling effects on the energy release rate of the crack for $\Psi = 0^\circ$. Again, the same decreasing effect of the latent heat in the plane strain condition

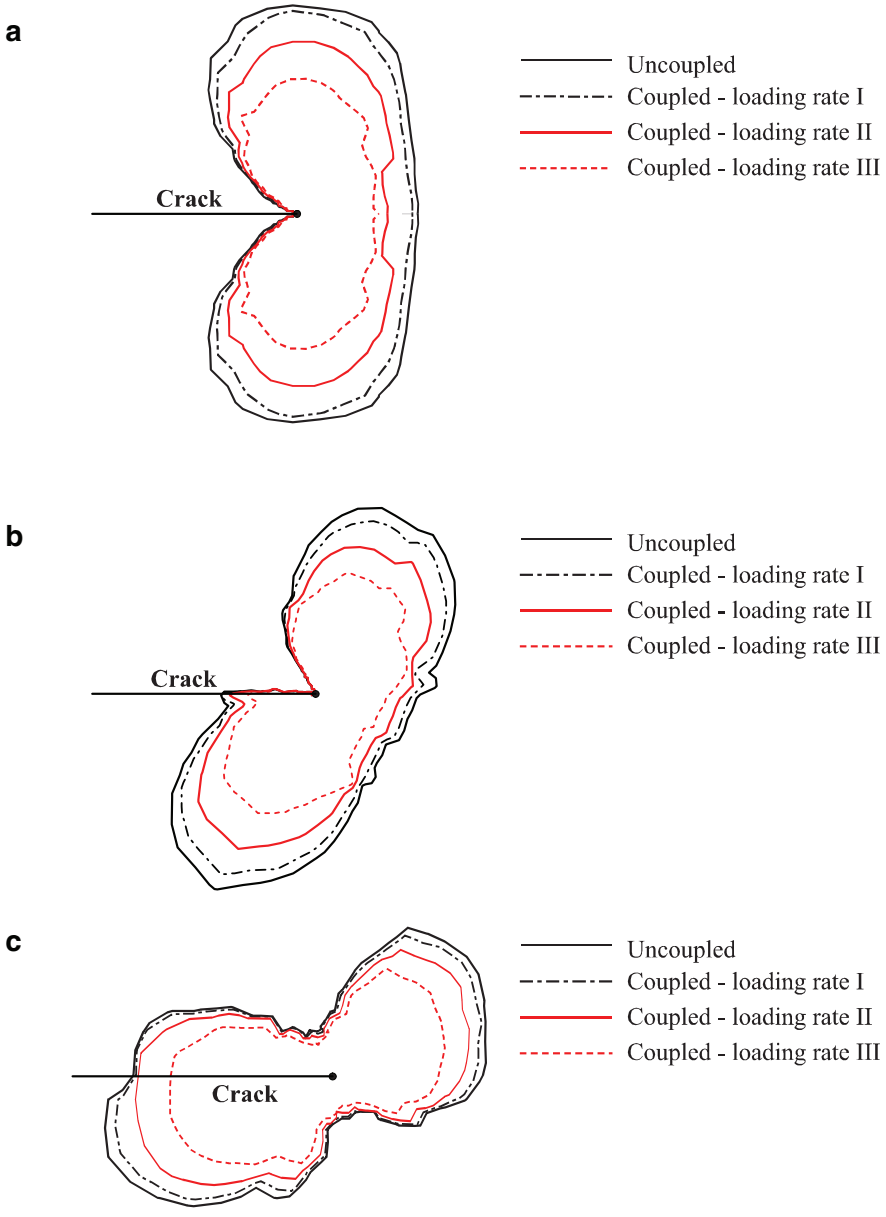

Fig. 24. Effect of applied loading rate on the shape of the transformation zone (a) $\Psi = 0^\circ$, (b) $\Psi = 15^\circ$, (c) $\Psi = 60^\circ$.

is observed here. Unlike Fig. 12, however, the critical distance, where the effect of applied strain rate becomes insignificant afterward, is much larger in the plane stress case. As an example, in pure mode-I plane strain condition, the critical distance is about $r/R_\xi = 0.04$, but in the plane stress condition this distance is about $r/R_\xi = 0.16$.

The thermo-mechanical coupling also affects the angular distribution of the temperature in points close to the crack tip. Fig. 22 shows that the temperature variations of a point located in $r/R_\xi = 0.0592$ for two cases of $\Psi = 0^\circ, 30^\circ$with different loading rates. As in the plane strain state, the variation becomes non-uniform in higher loading rates. However, due to the fact that the shape of the transformation zone differs in the plane stress case, the pattern of non-uniformity is different. In mode-I, for instance, in contrast to the plane strain case, the points behind the crack tip become colder. In plane stress state, the points in front of the crack have completely transformed and released the heat in an earlier time, whereas the points behind the crack remain in the partial transformation process in the last step of loading (see a zoomed-in contour in Fig. 23), and as a result, the released heat does not have sufficient time to reach the radius $r/R_\xi = 0.0592$ in high loading rates.

The dissimilarity in the shape of the transformation zone is also responsible for different angular distribution of temperature between plane stress and plane strain states in other mixed-mode conditions.

With respect to the effect of applied loading rate on the size–shape of the transformation zone (martensitic boundary ($\xi = 1$)), Fig. 24 is provided to show how increasing the rate of applied loading makes the zone smaller. Under slow loading rates, the forward phase transformation completes in lower level of strains, which gives a larger transformation zone. Zones of transformation for phase angles of $\Psi = 0^\circ$, $\Psi = 15^\circ$ and $\Psi = 60^\circ$ are depicted in Fig. 24 in order to show this phenomenon.

5. Conclusion

Performing plane stress and plane strain finite element analysis of thermo-mechanical coupling effects on mixed-mode crack tip fields in pseudoelastic shape memory alloys, increasing the rate of the applied loading releases more temperature in material points undergoing phase transformation, which in turn via the thermo-mechanical coupling effects results in decrease in the available energy for crack growth. Also, increasing the loading rate increases the stress during forward phase transformation, while making the size of the transformation zone smaller. With respect to angular distribution of the tip fields, the analysis demonstrated that the stress in partially transformed region is highly affected by the thermo-mechanical interaction in high loading rates. In a similar manner, temperature distribution of partially transformed regions is dissimilar to the fully transformed ones, especially in high loading rates. Differences in angular distribution of crack tip fields between plane stress and plane strain states, stemmed from different shapes of transformation zones, have also been examined and discussed.

Acknowledgments

The authors wish to acknowledge the technical support of the High Performance Computing Lab, School of Civil Engineering, and University of Tehran. The financial support of Iran National Science Foundation (INSF) is gratefully acknowledged.

References

Abeyaratne, R., Knowles, J.K., 1993. Continuum model of a thermoelastic solid capable of undergoing phase transformation. J. Mech. Phys. Solids 41, 541–571.
Ahmadian, H., Hatefi Ardakani, S., Mohammadi, S., 2015. Strain-rate sensitivity of unstable localized phase transformation phenomenon in shape memory alloys using a non-local model. Int. J. Solids Struct. 63, 167–183.
Anand, L., Gurtin, M.E., 2003. Thermal effects in the superelasticity of crystalline shape-memory materials. J. Mech. Phys. Solids 51, 1015–1058.
Auricchio, F., Taylor, R., Lubliner, J., 1997. Shape-memory alloys: macro-modeling and numerical simulations of the superelastic behavior. Comput. Methods Appl. Mech. Eng. 146, 281–312.
Baxevanis, T., Chemisky, Y., Lagoudas, D.C., 2012. Finite element analysis of the plane-strain crack-tip mechanical fields in pseudoelastic shape memory alloys. Smart Mater. Struct. 21, 094012.
Baxevanis, T., Lagoudas, D.C., 2012. A mode I fracture analysis of a center-cracked infinite shape memory alloy plate under plane stress. Int. J. Fract. 175, 151–166.
Baxevanis, T., Landis, C.M., Lagoudas, D.C., 2014. On the fracture toughness of pseudoelastic shape memory alloys. J. Appl. Mech. 81, 041005.
Bekker, A., Brinson, L.C., 1997. Temperature-induced phase transformation in a shape memory alloy: phase diagram based kinetics approach. J. Mech. Phys. Solids 45, 949–988.
Bo, Z., Lagoudas, D.C., 1999. Thermomechanical modeling of polycrystalline SMAs under cyclic loading, Part I: theoretical derivations. Int. J. Eng. Sci. 37, 1089–1140.
Boyd, J.G., Lagoudas, D.C., 1996. A thermodynamical constitutive model for shape memory materials. Part I. The monolithic shape memory alloy. Int. J. Plast. 12, 805–842.
Freed, Y., Banks-Sills, L., 2007. Crack growth resistance of shape memory alloys by means of a cohesive zone model. J. Mech. Phys. Solids 55, 2157–2180.
Gollerthan, S., Herberg, D., Baruj, A., Eggeler, G., 2008. Compact tension testing of martensitic/pseudoplastic NiTi shape memory alloys. Mater. Sci. Eng. A 481–482, 156–159.
Gollerthan, S., Young, M., K, N., Ramamurty, U., Eggeler, G., 2009. Direct physical evidence for the back-transformation of stress-induced martensite in the vicinity of cracks in pseudoelastic NiTi shape memory alloys. Acta Mater. 57, 5892–5897.
Gollerthan, S., Young, M.L., Baruj, A., Frenzel, J., Schmahl, W.W., Eggeler, G., 2009. Fracture mechanics and microstructure in NiTi shape memory alloys. Acta Mater. 57, 1015–1025.
Govindjee, S., Kasper, E.P., 1999. Computational aspects of one-dimensional shape memory alloy modeling with phase diagrams. Comput. Methods Appl. Mech. Eng. 171, 309–326.
Hatefi Ardakani, S., Ahmadian, H., Mohammadi, S., 2015. Thermo-mechanically coupled fracture analysis of shape memory alloys using the extended finite element method. Smart Mater. Struct. 24, 045031.
Helm, D., Haupt, P., 2003. Shape memory behavior: modelling within continuum thermomechanics. Int. J. Solids. Struct. 40, 827–849.
Lagoudas, D.C., 2008. Shape Memory Alloys: Modeling and Engineering Applications. Springer.
Lagoudas, D.C., Entchev, P.B., 2004. Modeling of transformation-induced plasticity and its effect on the behavior of porous shape memory alloys. Part I: constitutive model for fully dense SMAs. Mech. Mater. 36, 865–892.
Li, F.Z., Shih, C.F., Needleman, A., 1985. A comparison of methods for calculating energy release rates. Eng. Fract. Mech. 21, 405–421.
Lubliner, J., Auricchio, F., 1996. Generalized plasticity and shape memory alloys. Int. J. Solids Struct. 33, 991–1003.
Maletta, C., Bruno, L., Corigliano, P., Crupi, V., Guglielmino, E., 2014. Crack-tip thermal and mechanical hysteresis in shape memory alloys under fatigue loading. Mater. Sci. Eng. A 616, 281–287.
Maletta, C., Furgiuele, F., 2011. Fracture control parameters for NiTi based shape memory alloys. Int. J. Solids Struct. 48, 1658–1664.
Maletta, C., Sgambitterra, E., Furgiuele, F., 2013. Crack tip stress distribution and stress intensity factor in shape memory alloys. Fatigue Fract. Eng. Mater. Struct. 36, 903–912.
Paiva, A., Savi, M.A., Bragra, A.M.B., Pachec, P.M.C.L., 2005. A constitutive model for shape memory alloys considering tensile-compressive asymmetry and plasticity. Int. J. Solids Struct. 42, 3439–3457.
Popov, P., Lagoudas, D.C., 2007. 3-D constitutive model for shape memory alloys incorporating pseudoelasticity and detwinning of self-accommodated martensite. Int. J. Plast. 23, 1679–1720.
Qidwai, M.A., Lagoudas, D.C., 2000. Numerical implementation of a shape memory alloy thermomechanical constitutive model using return mapping algorithms. Int. J. Numer. Methods Eng. 47, 1123–1168.
Raniecki, B., Lexcellent, C., 1998. Thermodynamics of isotropic pseudoelasticity in shape memory alloys. Eur. J. Mech. A/Solids 17, 185–205.
Reese, S., Christ, D., 2008. Finite deformation pseudo-elasticity of shape memory alloys – constitutive modelling and finite element implementation. Int. J. Plast. 24, 455–482.
Robertson, S.W., Metha, A., Pelton, A.R., Ritchie, R.O., 2007. Evolution of crack-tip transformation zones in superelastic Nitinol subjected to in situ fatigue: a fracture mechanics and synchrotron X-ray micro-diffraction analysis. Acta Mater. 55, 6198–6207.
Stam, G., Van der Giessen, E., 1995. Effect of reversible phase transformations on crack growth. Mech. Mater. 21, 51–71.
Wang, G.Z., 2007. Effect of martensite transformation on fracture behavior of shape memory alloy NiTi in a notched specimen. Int. J. Fract. 146, 93–104.
Wang, X., Wang, Y., Baruj, A., Eggeler, G., Yue, Z., 2005. On the formation of martensite in front of cracks in pseudoelastic shape memory alloys. Mater. Sci. Eng. A 394, 393–398.
Xiong, F., Liu, Y., 2007. Effect of stress-induced martensitic transformation on the crack tip stress-intensity factor in Ni–Mn–Ga shape memory alloy. Acta Mater. 55, 5621–5629.
Yi, S., Gao, S., 2000. Fracture toughening mechanism of shape memory alloys due to martensite transformation. Int. J. Solids Struct. 37, 5315–5327.
Yi, S., Gao, S., Shen, S., 2001. Fracture toughening mechanism of shape memory alloys under mixed-mode loading due to martensite transformation. Int. J. Solids Struct. 38, 4463–4476.